JCB Journal of Cell Biology

TOOLS

An inducible multiciliated cell line resolves proteome dynamics and identifies CDK7 as a conserved regulator

Camille Boutin[1], Olivier Rosnet[1], Marine Touret[1], Stéphane Audebert[3], Luc Camoin[3], Salomé Dussert[1], Nicolas Brouilly[1], Virginie Thomé[1], Jean Plumail[2], Denis Fortun[2], Jean-Paul Borg[3,4], and Laurent Kodjabachian[1]

Multiciliated cells (MCCs) are essential for generating directional fluid flow across specialized epithelia in various vertebrate organs. MCC differentiation involves a tightly regulated program characterized by massive centriole amplification. Although transcriptional control of MCC development is well characterized, insights into proteome dynamics have been limited due to the lack of suitable models. Here, we report the generation of a stable inducible MCC line, derived from *Xenopus* A6 kidney epithelial cells. Upon induction of the master regulator multicilin (MCI), most A6-MCI cells synchronously differentiate into mature MCCs in 48 h. Using this resource, custom antibodies, and super-resolution imaging, we characterized *Xenopus* deuterosomes, the platforms that allow massive centriole synthesis in vertebrate MCCs. We performed detailed proteomic profiling throughout differentiation, uncovered previously uncharacterized regulators and highlighted a critical role for CDK7 in *Xenopus* and human MCC differentiation. Our work provides a valuable resource for mechanistic studies of MCC biology and opens avenues to identify novel therapeutic targets for motile ciliopathies.

Introduction

Multiciliated cells (MCCs) are widely present in the animal evolutionary tree and support major functions by generating physiological fluid flow at the surface of specialized epithelia through the beating of hundreds of cilia. In humans, MCCs are essential for the circulation of the cerebrospinal fluid in the central nervous system, in the transportation of gametes, and in the evacuation of soiled mucus from upper airways (Spassky and Meunier, 2017). Mutations that impair MCC differentiation or function cause severe multi-symptomatic diseases collectively referred to as motile ciliopathies (Wallmeier et al., 2020).

MCC differentiation is a highly regulated multistep process that can be described as an alternative cell cycle in which centriole amplification occurs uncoupled from DNA synthesis (Al Jord et al., 2017; Choksi et al., 2024; Serizay et al., 2025). MCCs synthesize almost simultaneously dozens to hundreds of centrioles using centriole-dependent and deuterosome-dependent pathways (Spassky and Meunier, 2017). Following amplification in the cytoplasm, centrioles move to the apical cell surface, gain appendages to allow linkage to the cortical cytoskeleton, and nucleate the formation of motile cilia (Boutin and Kodjabachian, 2019). Beyond similarities in the cellular mechanisms at play, it has become clear that, at various levels, regulatory pathways of MCC differentiation rely on intricate coordination between canonical cell cycle regulators and MCC-specific regulators. At the transcriptional level, two factors are related to the S phase regulator geminin: multicilin (MCI, encoded by the MCIDAS gene) and GemC, in complex with members of the E2F family of cell cycle transcriptional regulators, regulate the expression of a large body of effectors required for MCC differentiation (Kim et al., 2018; Lewis et al., 2023; Ma et al., 2014; Stubbs et al., 2012). MCI was reported to activate the expression of the transcription factor Myb, well known for its S phase promoting activity in a variety of progenitor cells. In MCCs, Myb is required for multiple centriole synthesis and, together with MCIDAS, for the activation of FoxJ1, a critical transcriptional regulator of motile ciliogenesis (Pan et al., 2014; Quigley and Kintner, 2017; Tan et al., 2013). Most of the centrioles in MCCs are produced by specialized structures called deuterosomes (Anderson and Brenner, 1971; Brenner, 1969; Kalnins and Porter, 1969; Sorokin, 1968; Steinman, 1968). The core of the deuterosome is

[1]Aix Marseille Univ, CNRS, IBDM, Turing Centre for Living Systems, Marseille, France; [2]CNRS, ICube, Université de Strasbourg, Illkirch, France; [3]Marseille Proteomics Platform, Centre de Recherche en Cancérologie de Marseille CRCM, Aix-Marseille Université, Inserm, CNRS, Institut Paoli-Calmettes, Marseille, France; [4]Institut Universitaire de France, Paris, France.

Correspondence to Camille Boutin: Camille.boutin@univ-amu.fr; Laurent Kodjabachian: laurent.kodjabachian@univ-amu.fr

O. Rosnet's current affiliation is Aix Marseille Univ, Inserm, CNRS, Institut Paoli Calmettes, CRCM, Marseille, France.

https://doi.org/10.1083/jcb.202506154

composed of the MCC-specific protein Deup1, a paralog of Cep63 (Zhao et al., 2013). Additional proteins such as pericentrin and γ-tubulin compose the peri-deuterosomal material (Revinski et al., 2018), and procentriole nucleation around deuterosomes involves many of the key players of the centriole duplication pathway, including PLK4, CEP152, and SAS6 (Al Jord et al., 2014; Klos Dehring et al., 2013; Zhao et al., 2013). At the end of the process, CDC20B—an MCC-specific protein related to the cell cycle protein CDC20—triggers a separase-dependent proteolytic event required for centriole disengagement from deuterosomes (Revinski et al., 2018).

The progression of MCCs through phases of differentiation is dependent on the cell cycle regulators CDK (Al Jord et al., 2017; Choksi et al., 2024; Serizay et al., 2025; Vladar et al., 2018). The mitotic oscillator, comprising CDK1 and APC/C, controls centriole synthesis and disengagement (Al Jord et al., 2017). CDK2 activity regulates both early phases of MCC differentiation and ciliogenesis (Vladar et al., 2018). CDK4 and CDK6, which are regulators of G1/S progression, are required to initiate MCC differentiation (Choksi et al., 2024).

Most of our knowledge on the molecular control of MCC differentiation is derived from bulk or single-cell transcriptomic approaches in *Xenopus*, mouse, and human (Ma et al., 2014; Redman et al., 2024; Revinski et al., 2018; Serizay et al., 2025). However, information on protein expression dynamics is critically missing, mainly due to the absence of model systems suitable for proteomic approaches.

In this study, we report the development of an inducible multiciliated cell line (A6-MCI). Building on the fact that MCI is necessary and sufficient to induce differentiation into MCCs of epithelial cells from *Xenopus* epidermis or mouse ependyma (Stubbs et al., 2012; Kyrousi et al., 2015), we demonstrate that the stable transfection of an inducible form of MCI is sufficient to drive differentiation into MCCs of A6, a cell line derived from the kidney of the South African clawed toad, *Xenopus laevis* (Rafferty, 1969). The A6-MCI line has a high differentiation rate and is very homogeneous, making it an ideal tool for advanced microscopy and proteomics approaches. Using this unique resource, we further characterized the organization of *Xenopus* MCC deuterosomes, revealing similar as well as unique features when compared with mammalian MCCs. We assembled the proteome of MCCs at different stages of differentiation, which revealed several uncharacterized regulators that may contribute to key functions in MCC biology. Highlighting the value of this unique dataset, we uncovered the importance of CDK7 activity for the differentiation of *Xenopus* and human MCCs.

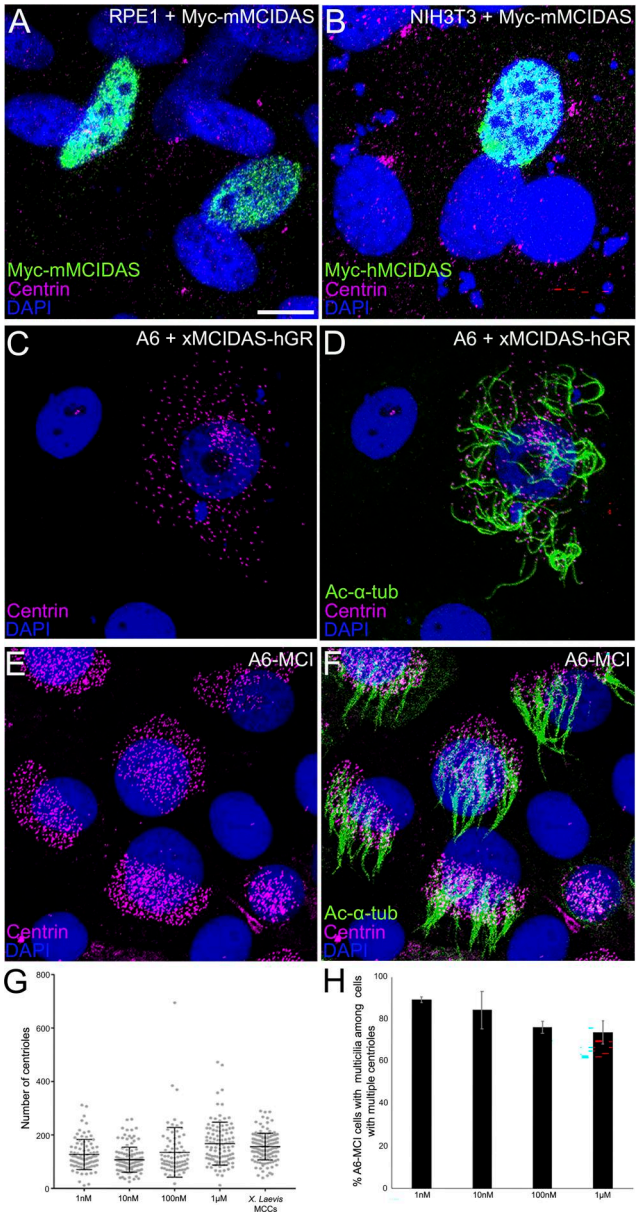

Figure 1. **MCI expression in A6 cells drives differentiation in MCCs. (A–D)** Confocal pictures of RPE1 (A), NIH3T3 (B), and A6 (C and D) cells transiently transfected with Myc-mMCIDAS or XMCIDAS-hGR and immunostained for the indicated markers. **(E and F)** Confocal pictures of stably transfected A6-MCI cells stained for the indicated markers. **(G)** Quantification of centriole number per cell in A6-MCI cells induced with increasing concentrations of dexamethasone and in *X. laevis* epidermal MCCs. Mean and SD are shown. *n* = 91 cells (1 nM), 124 cells (10 nM), 80 cells (100 nM), 103 cells (1 μM), and 155 cells (*X. laevis*). Data were collected from one experiment. **(H)** Percentage of A6-MCI cells with multicilia among those with multiple centrioles. Error bars are SD. *n* = 936 (1 nM), 1277 (10 nM), 1432 (100 nM), and 1282 (1 μM) cells. Data collected from two experiments. Scale bar: 10 μm (A–D), 13 μm (E and F).

Results

MCI expression is sufficient to drive differentiation of A6 cells into MCCs

In an attempt to generate an MCC line, we tested whether forced MCIDAS expression alone could trigger MCC differentiation in established vertebrate cell lines. We first transfected RPE1 and NIH3T3 cells with mouse MCIDAS and analyzed their differentiation using centriole and cilium markers. We observed that neither cell line was responsive to MCIDAS expression alone (Fig. 1, A and B). Next, we transfected A6 *X. laevis* cells with *X. laevis* MCIDAS fused to the ligand-binding domain of the human glucocorticoid receptor (xMCIDAS-hGR). This inducible form of MCIDAS is retained in the cytoplasm until dexamethasone is added to the culture medium (Stubbs et al., 2012). Observation of

the culture 24 h after dexamethasone treatment revealed amplified centrioles and multiple cilia, showing that expression of MCIDAS alone was sufficient to induce A6 cells into MCCs (Fig. 1, C and D). In the next step, we stably transfected A6 cells with xMCIDAS-hGR. After selection and cloning by limit dilution, we obtained the A6-MCI cell line. 72 h post induction (hpi) with dexamethasone, A6-MCI MCCs were fully differentiated with multiple centrioles and cilia at their apical surface (Fig. 1, E and F). To define the best induction protocol, we compared differentiation rates in the cultures at 72 hpi with increasing concentrations of dexamethasone applied for either 8 or 24 h. In the case of a short induction (8 h), the number of cells with multiple centrioles increased proportionally to the amount of dexamethasone added, ranging from 20% at 1 nM to above 60% at 1 µM (Fig. S1, A and C). In the case of a prolonged induction (24 h), differentiation levels were more comparable (over 50% at 1 nM, up to 70% at 1 µM) (Fig. S1, A and D). Similar results were observed at 1 week after induction, suggesting that the maximum of differentiation is reached by 72 h (Fig. S1, A and E). Of note, no signs of differentiation were observed in non-induced (NI) A6-MCI cultured for 72 h or 1 week (Fig. S1 B), suggesting that dexamethasone control of induction is robust and that there is no leakage in the system. No major differences were observed in the number of centrioles generated by individual MCCs with the different dexamethasone concentrations, and those numbers were comparable with those of native *Xenopus* epidermal MCCs (Fig. 1 G). Finally, we observed that in all conditions, over 80% of cells that undergo centriole amplification also make multicilia (Fig. 1 H). Following these analyses, induction for 24 h with 100 nM dexamethasone was selected as the routine condition.

Altogether, these results demonstrate that the stable expression of MCIDAS is sufficient to induce a rapid, robust, and reproducible differentiation of A6 cells into MCCs.

A6-MCI differentiation is synchronous and recapitulates the main features of MCCs

To further characterize the A6-MCI line, we performed a time course analysis to define the main steps of their differentiation. As MCC differentiation starts with centriole synthesis, we aimed at analyzing the expression of Deup1, which constitutes the core of vertebrate deuterosomes, the platforms where massive centriole assembly occurs. For this, we raised and characterized a rabbit polyclonal antibody against *Xenopus* Deup1, which proved to give specific signals in both western blotting and immunofluorescence (Fig. 2, A–C and Fig. S2). In western blots of A6-MCI cells, Deup1 was first detected at 8 hpi, increased to reach a plateau at 24 hpi, before declining in mature MCCs (Fig. S2 C). As expected, the increase in expression of the centriole marker centrin was delayed compared with Deup1. While low basal expression was detected in NI and at 8 hpi, centrin strongly increased from 12 hpi up to 48 hpi and then remained stable (Fig. S2 C). Finally, the acetylated form of alpha-tubulin (Ac-α-Tub), a cilia component, increased from baseline levels in NI cells to reach maximum levels at 72 hpi and remained stable up to one week after induction (Fig. S2 C). Next, we performed immunostainings to characterize the state of MCC differentiation at different times after induction. At 8 hpi, although western blot data showed that the differentiation program was engaged, induced and NI cells appeared similar with respect to deuterosome (Deup1) and centriole (centrin) markers (Fig. 2, A, B, and J). At 16 hpi, over 50% of induced cells were engaged in the phase of centriole amplification as shown by the accumulation of structures positive for Deup1, γ-tubulin, pericentrin, and centrin, corresponding to deuterosomes bearing pro-centrioles (Fig.2, C, J, and K; Fig. S2 D; and Fig. S3). At 24 hpi, centriole amplification was almost completed, as shown by the decrease in the number of cells with deuterosomes and the increase in the number of cells with released centrioles (Fig. 2, D–F, J, and K). In most cells, individual centrioles were transforming into basal bodies, as shown by the presence of γ-tubulin and Cep164 - respective markers of the basal foot and distal appendages—juxtaposed to centrin (Fig. 2, E and F). At 24 hpi, although cilia were not grown, IFT88 started to accumulate at basal bodies in a subset of cells (Fig. S3). At 48 hpi, a majority of cells presented cilia at their apical surface (Fig. 2, G and K). Accordingly, ciliary pools of IFT88 were observed, indicating active transport into cilia (Fig. 2 H). In addition, Ruvb2-positive Dynaps, which have been described as condensates enabling the association of dynein arms prior to their import into cilia (Huizar et al., 2018), were observed in most of the cells (Fig. 2 I). Finally, at 72 hpi, deuterosomes and Dynaps were no longer observed, and most cells presented mature centrioles and were ciliated (Fig. 2 K and Fig. S3).

Next, we used high-resolution imaging to better assess the structures of centrioles and cilia in A6-MCI MCCs. Ultrastructure expansion microscopy (UExM) revealed the expected distal position of centrin within the space delineated by centriole walls, marked by Ac-α-Tub (Fig. 3 A). UExM also confirmed the ninefold distribution of Cep164-positive distal appendages, as well as the asymmetric position of the γ-tubulin–positive basal foot (Fig. 3, B–D). We further analyzed A6-MCI centrioles using transmission electron microscopy (TEM). As classically observed in MCCs, A6-MCI centrioles presented nine microtubule triplets and were decorated with a basal foot linked to cytoplasmic microtubules, nine distal appendages, and rootlets (fan-shaped or long and slim, like in *Xenopus* epidermal MCCs), demonstrating their proper maturation in basal bodies (BBs) (Fig. 3, E–H). In mature A6-MCI cells, BBs were unsheathed in apical actin fibers and nucleated microtubules (Fig. 3, I–L), similar to natural *Xenopus* epidermal MCCs (Boutin et al., 2014; Werner et al., 2011). However, we noticed that A6-MCI cells did not coordinate BB orientation as MCCs normally do *in vivo* (Fig. 3, M–O). To evaluate whether A6-MCI MCCs are empowered with metachronal beating capacity, we tested if they could generate fluid flows. For this, we recorded the movement of fluorescent beads released on the surface of differentiated A6-MCI cultures. We did not detect any active movement of the beads, but only diffusion, suggesting the absence of ciliary beating (Video 1). We thus tested whether ectopic expression of MCI-hGR in *Xenopus* epidermis promoted beating in induced MCCs. As expected, MCI expression induced the transformation of most superficial epidermal cells into MCCs (Stubbs et al., 2012; Video 2). However, MCI-induced ectopic MCCs failed to beat, contrary to control cells (Video 2).

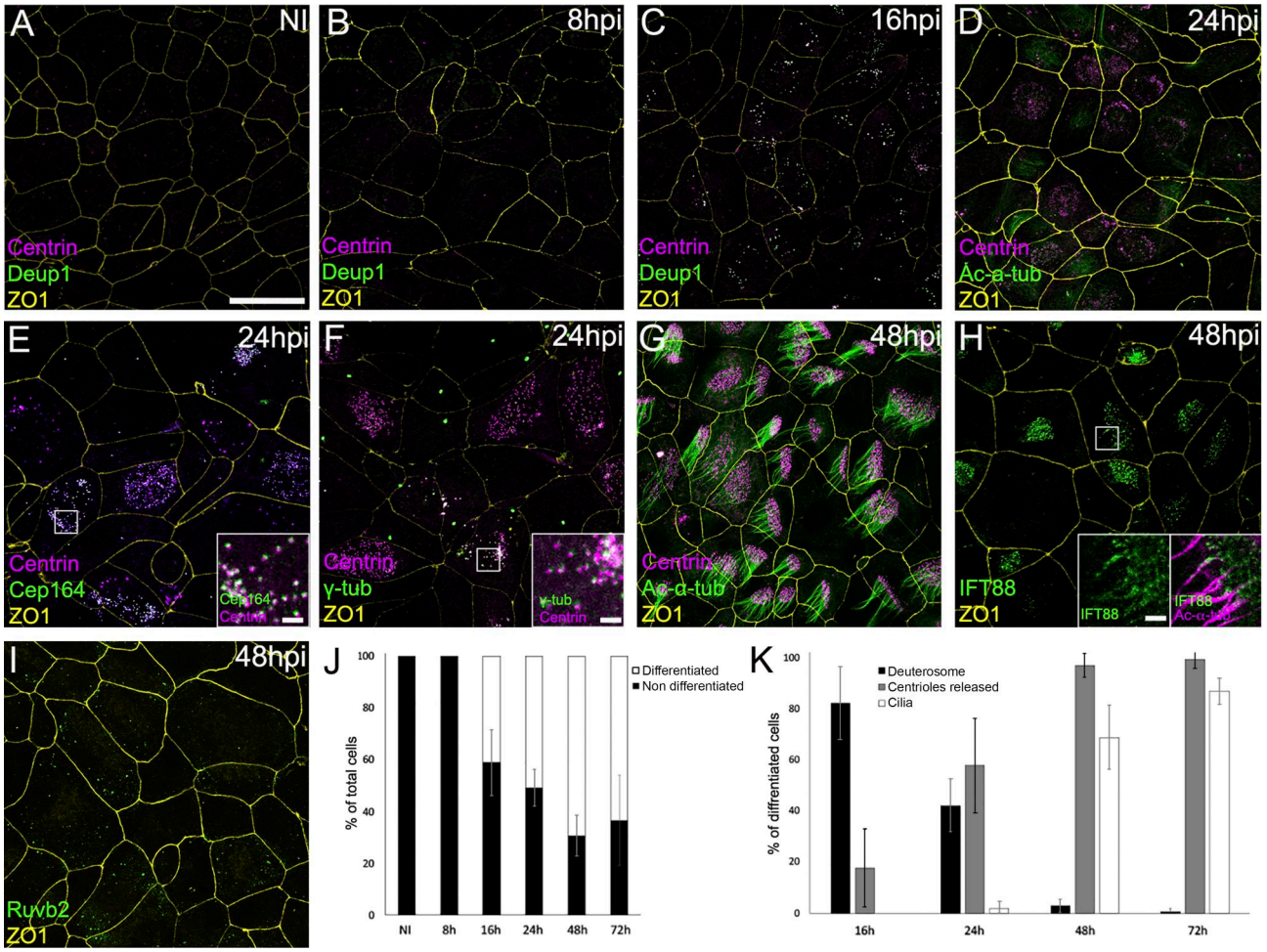

Figure 2. **A6-MCI cells recapitulate the main differentiation steps of MCCs. (A–I)** Confocal pictures of NI (A) or induced A6-MCI cells (B–I) at indicated hpi stained for the indicated markers. **(J)** Bar graph quantification of non-differentiated cells and differentiated cells at the indicated times after induction. For the stages NI, 8 h, and 16 h, cell differentiation was evaluated by the presence of Deup1 and centrin labelling. For the stages 24 h, 48 h, and 72 h, cell differentiation was evaluated by the presence of centrin labelling. Error bars are SD. *n* = 414 (NI), 456 (8 h), 293 (16 h), 288 (24 h), 478 (48 h), and 373 (72 h) cells. Data were collected from three independent experiments. **(K)** Bar graph showing the distribution of differentiated cells at 16 hpi, 24 hpi, and 72 hpi in deuterosome, centriole released, and ciliated categories evaluated by Deup1/centrin (see Fig. S3 C) and centrin/Ac-α-Tub staining, respectively. Error bars are SD. *n* = 115 (16 h), 288 (24 h), 148 (48 h), and 330 (72 h) cells. Data were collected from three independent experiments. Scale bar: 30 µm (A–I); 2.5 µm (E–G, inset).

Altogether, these results show that over 70% of A6-MCI–induced cells recapitulate the main steps of MCC differentiation in a precisely timed manner, although cilia polarity and motility appear to need additional levels of control.

Xenopus deuterosomes exhibit a distinctive organization

In vertebrate MCCs, deuterosomes support the production of most centrioles (Spassky and Meunier, 2017). In the *Xenopus* embryonic epidermis, cells at the deuterosomal stage are localized in the inner layer and represent about 10% of the cells present in the tissue, which makes high-resolution imaging of the sub-micrometric deuterosome organelle challenging (Boutin and Kodjabachian, 2019). Thus, we decided to use the A6-MCI model to investigate the molecular and architectural organization of *Xenopus* deuterosomes. We first analyzed with confocal microscopy the respective distribution of Deup1 and centrin signals in deuterosomal cells. Consistent with our previously published observations (Revinski et al., 2018), the deuterosomes of both A6-MCI MCCs and *Xenopus* epidermal MCCs showed irregular shapes and sizes (Fig. 4, A and B). We then analyzed the distribution of γ-tubulin and pericentrin, two proteins that we had previously identified as being associated with the deuterosome of *Xenopus* epidermal and mouse ependymal MCCs (Revinski et al., 2018). Confocal immunofluorescence confirmed that those proteins localized to A6-MCI deuterosomes associated with centrin-positive centrioles (Fig. 4, C and D). Together, these results suggest that A6-MCI deuterosomes are similar to those observed in natural *Xenopus* MCCs. Interestingly, although the shapes of deuterosomes differ between mouse ependymal and *Xenopus* MCCs, STED super-resolution microscopy analysis on A6-MCI MCCs revealed that the relative positions of markers are conserved, with Deup1 being central, γ-tubulin, and pericentrin being more peripheral in that order (Fig. S4 A; [Revinski et al., 2018]).

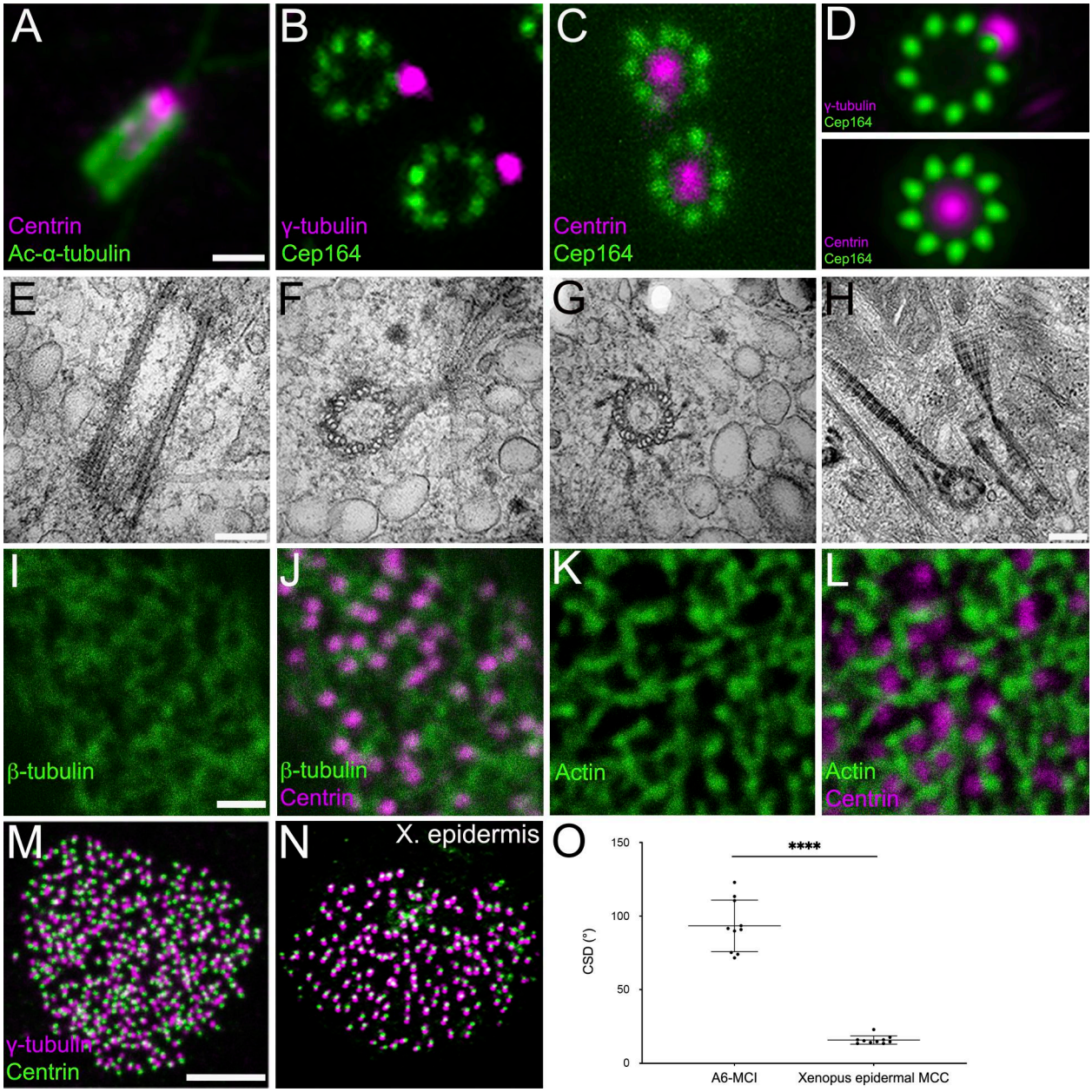

Figure 3. **Basal bodies in A6-MCI cells. (A–C)** Confocal pictures of basal bodies of expanded differentiated A6-MCI cells stained for Ac-α-Tub (microtubules) and centrin (centriole lumen) (A), γ-tubulin (basal foot) and Cep164 (distal appendages) (B), or Cep164 and centrin (C). **(D)** Average map distribution of indicated markers. **(E–H)** TEM pictures from differentiated A6-MCI cells. **(E)** Lateral view of a basal body. **(F)** Top view of a basal body displaying 9 microtubule triplets and a basal foot nucleating individual cytoplasmic microtubule. **(G)** Top view of a basal body displaying 9 microtubule triplets and distal appendages. **(H)** View of basal bodies showing fan-shaped or long rootlets. **(I and J)** Confocal pictures of mature A6-MCI cells apical surface stained for β-tubulin (microtubules) and centrin (centrioles). **(K and L)** Confocal pictures of mature A6-MCI cells apical surface stained for actin and centrin (centrioles). **(M and N)** Confocal pictures of 72 hpi A6-MCI (M) and *X. laevis* epidermal MCCs (N) stained for centrin (centriole) and γ-tubulin (basal foot) reveal the polarity of basal bodies. **(O)** Quantification of basal body circular SD (CSD) in A6-MCI and *X. laevis* epidermal MCCs. Mean and SD are shown. *n* = 10 cells per condition. Data collected from one experiment. Unpaired *t* test with Welch's correction: P < 0.0001 (****). Scale bar: 250 nm (A–C); 150 nm (E–G); 200 nm (H); 1 µm (I–L); 5 µm (M–O).

Next, we used fourfold magnification UExM to further analyze the shape of deuterosomes in A6-MCI cells. Three major shapes were observed: short deuterosomes with a central Deup1-positive core of ∼300–400 nm bearing 2 to 6 procentrioles (Fig. 4 E); long deuterosomes, which presented a linear core between 1.75 and 3.15 µm long and carried 18 to 28 procentrioles (Fig. 4 F); and finally, larger deuterosomal structures with Deup1-positive ramified segments (Fig. 4 G). Deuterosomes with globular cores were occasionally observed (Fig. 4 H). Upon closer observation, long deuterosomal entities appeared to be formed of juxtaposed spheroid Deup1-positive units. To extend this analysis, we processed A6-MCI cells for serial TEM. Using this approach, we

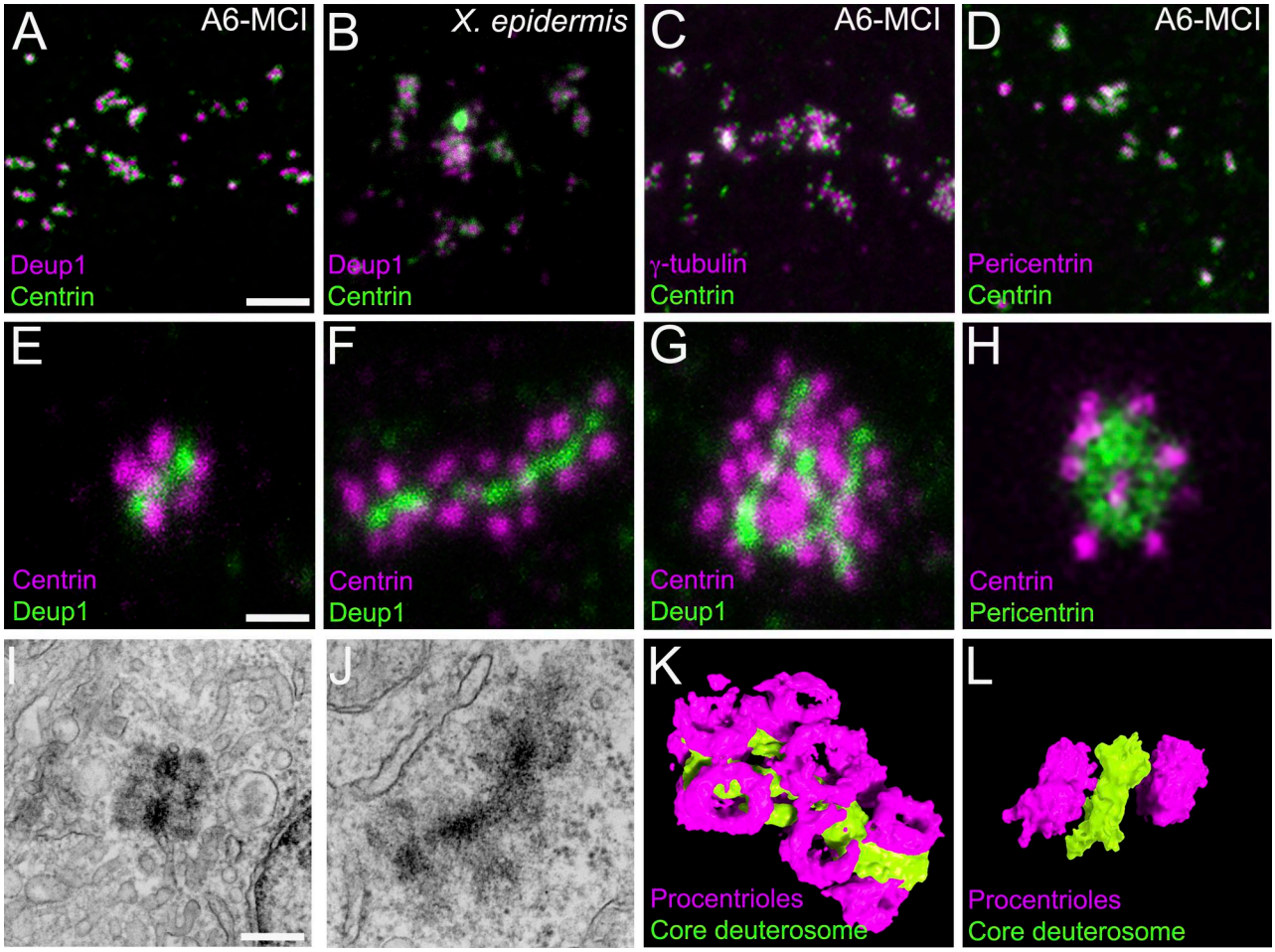

Figure 4. **Deuterosome organization in A6-MCI cells. (A–D)** Confocal pictures of 16 hpi A6-MCI (A, C, and D) or *Xenopus* epidermis (B) MCCs stained with the indicated deuterosome (Deup1, pericentrin, and γ-tubulin) or centriole (centrin) markers. **(E–G)** Expansion microscopy confocal picture of short (E), long (F), and ramified (G) A6-MCI deuterosomes stained for Deup1 and centrin. (H) STED super-resolution microscopy picture of globular A6-MCI deuterosomes stained with pericentrin and centrin. **(I and J)** TEM pictures of A6-MCI deuterosomes. J picture is duplicated in Fig. S4 B. **(K and L)** Segmentation obtained from tomogram acquisition of ramified (K) and short (L) A6-MCI deuterosomes. Scale bar: 2.5 µm (A–D); 280 nm (E–H); 225 nm (I and J).

could observe small deuterosomes loaded with few procentrioles, restricted to one section (thickness = 70 nm), as well as long deuterosomes spanning several consecutive sections (Fig. 4, I and J; Fig. S4 B). However, the serial TEM approach did not allow us to precisely reconstruct the 3D structure of deuterosomes spanning more than one section. Therefore, we turned to serial tomography, which allows the reconstruction of EM volumes at high and isotropic resolution. With this approach, we were able to reconstruct in 3D small, long, and ramified structures, thereby confirming the existence of various deuterosomal architectures (Fig. 4, K and L; and Videos 3, 4, and 5). Importantly, ultrastructure analysis with TEM and tomography confirmed the "string of pearls" organization of deuterosomal platforms, revealed by UExM. Regardless of the size or general shape of deuterosomal platforms, most of them appeared as a series of electron-dense spheroid (86 ± 14 nm diameter) connected by thinner material, each bearing two to three procentrioles. Altogether, these results show that A6-MCI cells contain deuterosomes similar to those of *Xenopus* epidermal MCCs. High-resolution imaging also suggests that deuterosomes of *Xenopus* MCCs are composed of small spherical units that can be linked to generate supra-structures of variable length and geometry.

Temporal proteomic analysis of MCC differentiation

The results presented above indicate that the A6-MCI cell line recapitulates MCC differentiation with high fidelity. To further characterize this progression, we performed mass spectrometry analysis to define the list of proteins expressed in NI cells and at 8, 16, 24, 48, and 72 h after induction (Table S1). Principal component analysis of mass spectrometry data revealed that samples were separated according to time after induction, confirming sequential, synchronous, and reproducible differentiation of A6-MCI cells (Fig. 5 A). We then analyzed the difference in protein expression between successive time points (Table S1). Consistent with the absence of major signs of differentiation in immunofluorescence, little change in protein expression was observed between NI and 8 h (Fig. 5 B). The number of proteins upregulated between successive time points gradually increased from 8 to 48 h, reflecting the progression into the different phases of differentiation of induced A6-MCI cells (Fig. 5, C–E). In

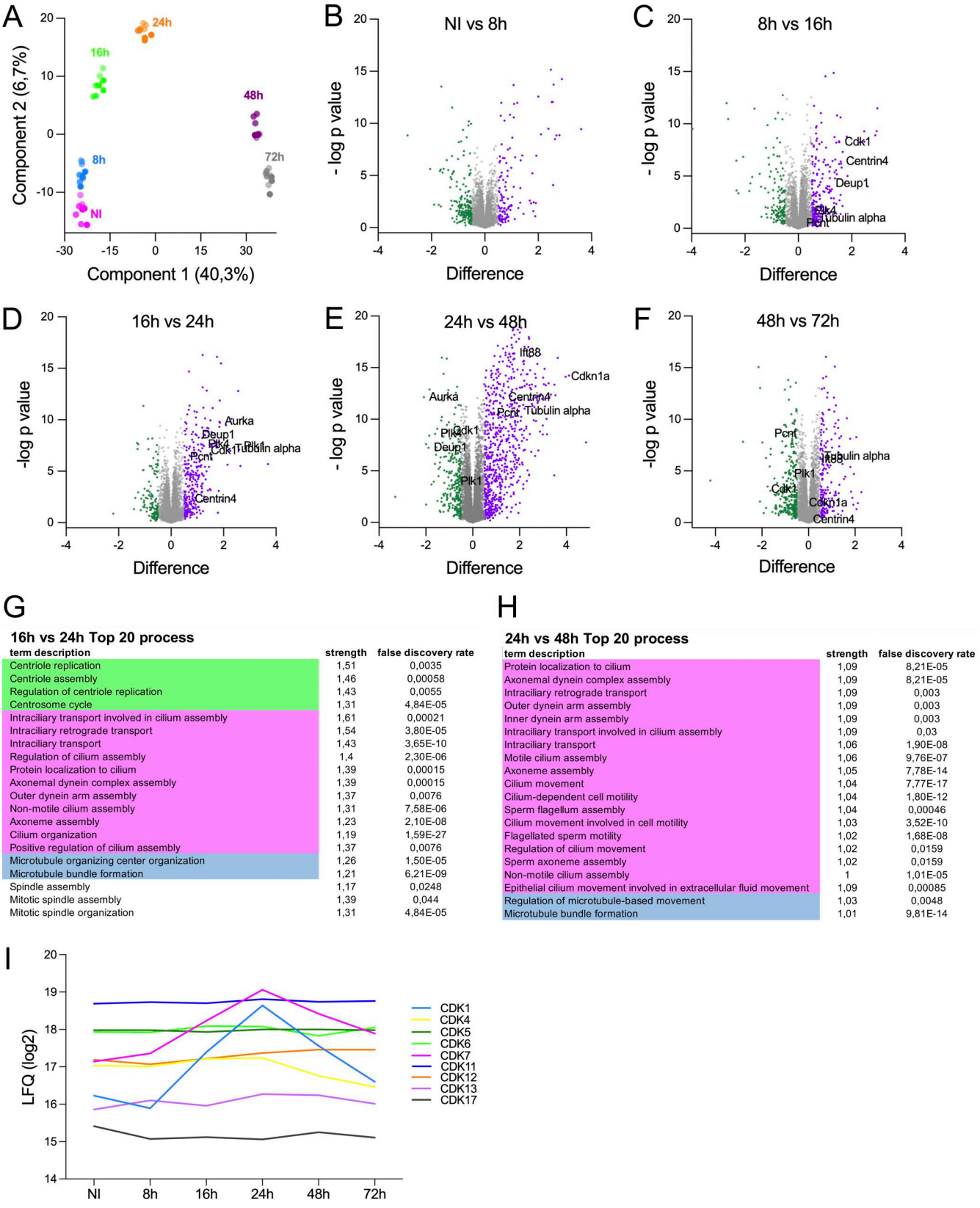

G

16h vs 24h Top 20 process

term description	strength	false discovery rate
Centriole replication	1,51	0,0035
Centriole assembly	1,46	0,00058
Regulation of centriole replication	1,43	0,0055
Centrosome cycle	1,31	4,84E-05
Intraciliary transport involved in cilium assembly	1,61	0,00021
Intraciliary retrograde transport	1,54	3,80E-05
Intraciliary transport	1,43	3,65E-10
Regulation of cilium assembly	1,4	2,30E-06
Protein localization to cilium	1,39	0,00015
Axonemal dynein complex assembly	1,39	0,00015
Outer dynein arm assembly	1,37	0,0076
Non-motile cilium assembly	1,31	7,58E-06
Axoneme assembly	1,23	2,10E-08
Cilium organization	1,19	1,59E-27
Positive regulation of cilium assembly	1,37	0,0076
Microtubule organizing center organization	1,26	1,50E-05
Microtubule bundle formation	1,21	6,21E-09
Spindle assembly	1,17	0,0248
Mitotic spindle assembly	1,39	0,044
Mitotic spindle organization	1,31	4,84E-05

H

24h vs 48h Top 20 process

term description	strength	false discovery rate
Protein localization to cilium	1,09	8,21E-05
Axonemal dynein complex assembly	1,09	8,21E-05
Intraciliary retrograde transport	1,09	0,003
Outer dynein arm assembly	1,09	0,003
Inner dynein arm assembly	1,09	0,003
Intraciliary transport involved in cilium assembly	1,09	0,03
Intraciliary transport	1,06	1,90E-08
Motile cilium assembly	1,06	9,76E-07
Axoneme assembly	1,05	7,78E-14
Cilium movement	1,04	7,77E-17
Cilium-dependent cell motility	1,04	1,80E-12
Sperm flagellum assembly	1,04	0,00046
Cilium movement involved in cell motility	1,03	3,52E-10
Flagellated sperm motility	1,02	1,68E-08
Regulation of cilium movement	1,02	0,0159
Sperm axoneme assembly	1,02	0,0159
Non-motile cilium assembly	1	1,01E-05
Epithelial cilium movement involved in extracellular fluid movement	1,09	0,00085
Regulation of microtubule-based movement	1,03	0,0048
Microtubule bundle formation	1,01	9,81E-14

Figure 5. **Proteomic analysis of A6-MCI cells. (A)** PCA analysis of the complete the proteomic dataset. **(B–F)** Volcano plots of differential expression analysis between the indicated times after induction. Log2 difference in expression between time points and −log P value are plotted. Upregulated proteins with a Log2 difference of >0.5 are shown in purple. Downregulated proteins with a Log2 difference less than −0.5 are shown in green. Ni vs 8 h: 125 up, 194 down; 8 vs 16 h: 222 up, 137 down; 16 vs 24 h: 301 up, 124 down; 24 vs 48 h: 699 up, 270 down; 48 vs 72 h: 187 up, 298 down. **(G and H)** Top 20 GO term processes associated with 16–24 h (G) and 24–48 h (H) transitions. **(I)** Graph showing the variation of expression of all Cdks detected in the proteomic dataset using the LFQ intensity. PCA, principal component analysis.

contrast, between 48 and 72 h, the differences in proteomes were less significant (Fig. 5 F), as expected since a majority of induced cells have completed ciliogenesis at 48 hpi (Fig. 2, J and K). The 8–16 h transition clearly revealed the engagement into the phase of centriole synthesis, with upregulation of Cdk1, Deup1, Plk4, and centrin 4 (Fig. 5 C). Between 16 and 24 h, we noticed the upregulation of Plk1, which is known to be involved in centriole disengagement from the deuterosomes (Revinski et al., 2018). This transition thus marked the termination of the centriole production phase (Fig. 5 D). The 24–48 h transition revealed the downregulation of Cdk1, Deup1, and Plk4, concomitantly to the upregulation of Cdkn1a, the negative regulator of Cdk1 and Ift88 (Fig. 5 E). Those changes are indeed compatible with the transition from centriole synthesis to ciliogenesis phases. To generate a more global overview of our dataset, we analyzed the top 20 gene ontology (GO) terms that describe the proteins significantly upregulated at the 16–24 h and 24–48 h transitions. The 16–24 h transition was characterized by the presence of 4 GO terms related to centriole biogenesis and 11 terms related to cilia assembly (Fig. 5 G). In the 24–48 h transition, all centriole biogenesis GO terms were lost, and 18/20 terms were related to cilia assembly and motility (Fig. 5 H). Overall, the data described above indicate that the A6-MCI system is amenable to proteomic analyses, as its level of synchrony is sufficient to distinguish the multiple phases of the alternative cell cycle at play in MCCs (Al Jord et al., 2017; Choksi et al., 2024; Serizay et al., 2025).

In an attempt to identify novel regulators of the MCC alternative cycle, we focused our attention on members of the CDK family detected in the proteomes. We could detect 9 Cdks with two distinct temporal expression profiles (Fig. 5 I). On the one hand, Cdk1 and Cdk7 showed dynamic and parallel expression, increasing during the phase of centriole synthesis (16–24 h), before decreasing during the ciliogenesis phase (24–72 h) (Fig. 5 I). On the other hand, Cdk4, Cdk6, Cdk5, Cdk11, Cdk12, Cdk13, and Cdk17 showed stable expression levels between the different stages of differentiation (Fig. 5 I). Among the Cdk members detected in our dataset, Cdk1, Cdk4, and Cdk6 have been shown to regulate the MCC alternative cell cycle (Al Jord et al., 2017; Choksi et al., 2024; Vladar et al., 2018). Next, we analyzed whether Cdk7, the expression of which matches that of Cdk1, is important for MCC biogenesis.

CDK7 plays a conserved role in differentiating MCCs

In *Xenopus*, Cdk7 was shown to be a direct transcriptional target of MCI (Ma et al., 2014). CDK7 in association with cyclin H (CCNH) and MAT1A drives cell cycle progression by promoting the activity of CDK1, 2, 4, and 6 (Fisher, 2005), which have all been involved in the MCC alternative cycle (Al Jord et al., 2017; Choksi et al., 2024; Vladar et al., 2018). We tested the involvement of CDK7 in the alternative cell cycle of MCCs using chemical and knockdown approaches. Strikingly, the application of CDK7 inhibitors (YKL-5-124 and LDC4297) on A6-MCI cells at the time of induction almost totally prevented MCC differentiation (Fig. 6, A–D). To probe the validity of this result *in vivo*, we analyzed epidermal MCC from *Xenopus* embryos cultured in the presence of CDK7 inhibitors. Control embryos showed homogeneously distributed, fully ciliated MCCs. In contrast, embryos treated with LDC4297 or YKL-5-124, although containing correct numbers of MCCs, showed severe differentiation defects, with most cells failing to generate centrioles and cilia (Fig. 6, E–H). Importantly, injection of two distinct Cdk7 morpholinos also prevented centriole and cilium biogenesis in epidermal MCCs (Fig. 6, I–L). Taken together, our results establish the critical role of Cdk7 in *Xenopus* MCCs. Next, we explored at what stage of the differentiation cascade Cdk7 was necessary. When either of the CDK7 inhibitors was added on A6-MCI at 8 hpi, MCC differentiation was greatly suppressed, to a rate comparable with that observed when inhibition started at induction. Cdk7 inhibition from 16 hpi impaired MCC differentiation to a lower extent. Finally, when the drugs were added at 24 h or 48 h, no difference was observed compared with the control situation, suggesting that cells produced centrioles and cilia normally (Fig. S5 A). Similarly, when the drug YKl-5-124 was added to *Xenopus* early gastrula (St 10) embryos, MCCs did not produce centrioles and cilia, whereas when the drug was added between the centriologenesis and ciliogenesis phases (St 20), no major defects were observed (Fig. S5 B). These results ruled out toxicity and confirmed the involvement of Cdk7 at an early phase of MCC biogenesis, as suggested by the proteomic analysis. Published single-cell transcriptomic data reveal that *CDK7*, *CCNH*, and *MAT1* are also expressed in the MCC lineage of human airway epithelial cell cultures (hAECs) (Redman et al., 2024). To evaluate the importance of CDK7 in the biogenesis of human MCCs, we applied CDK7 inhibitors on air–liquid hAECs at air–liquid interface (ALI) day 0, when differentiation starts. Here again, both LDC4297 and YKL-5-124 nearly totally abolished MCC differentiation (Fig. 6, M–P). Together, these results indicate that CDK7 plays a crucial role at an early step of MCC differentiation, which is conserved from *Xenopus* to human.

Discussion

In this study, we report the generation of the A6-MCI cell line that can be induced in a controlled manner to generate MCCs. We show that this cell line recapitulates the main characteristics of MCCs observed *in vivo*. Using this cell line, we characterized *Xenopus* deuterosomes and provided an unprecedented description of their molecular organization. We also assembled the dynamic proteome of MCCs, a unique resource that will help to identify key regulators and effectors of MCC biogenesis. As proof of principle, we demonstrate that the uncharacterized kinase CDK7 is of critical importance for MCC differentiation in *Xenopus* and humans.

Comparison between MCCs of the *Xenopus* epidermis and the A6-MCI cell line showed that both amplify their centrioles via deuterosomes that have comparable architectures. It also highlighted differences with deuterosomes of other MCC subtypes. In mouse ependymal cells, deuterosomes appear as individual spheres of uniform size bearing typically 15 procentrioles, whereas in mouse tracheal MCCs, deuterosomes appear as individual spheres of variable size bearing a variable number of procentrioles. Here, an in-depth analysis using expansion microscopy, TEM, and tomography reveals that deuterosomal platforms in *Xenopus* MCCs consist of individual spheres loaded

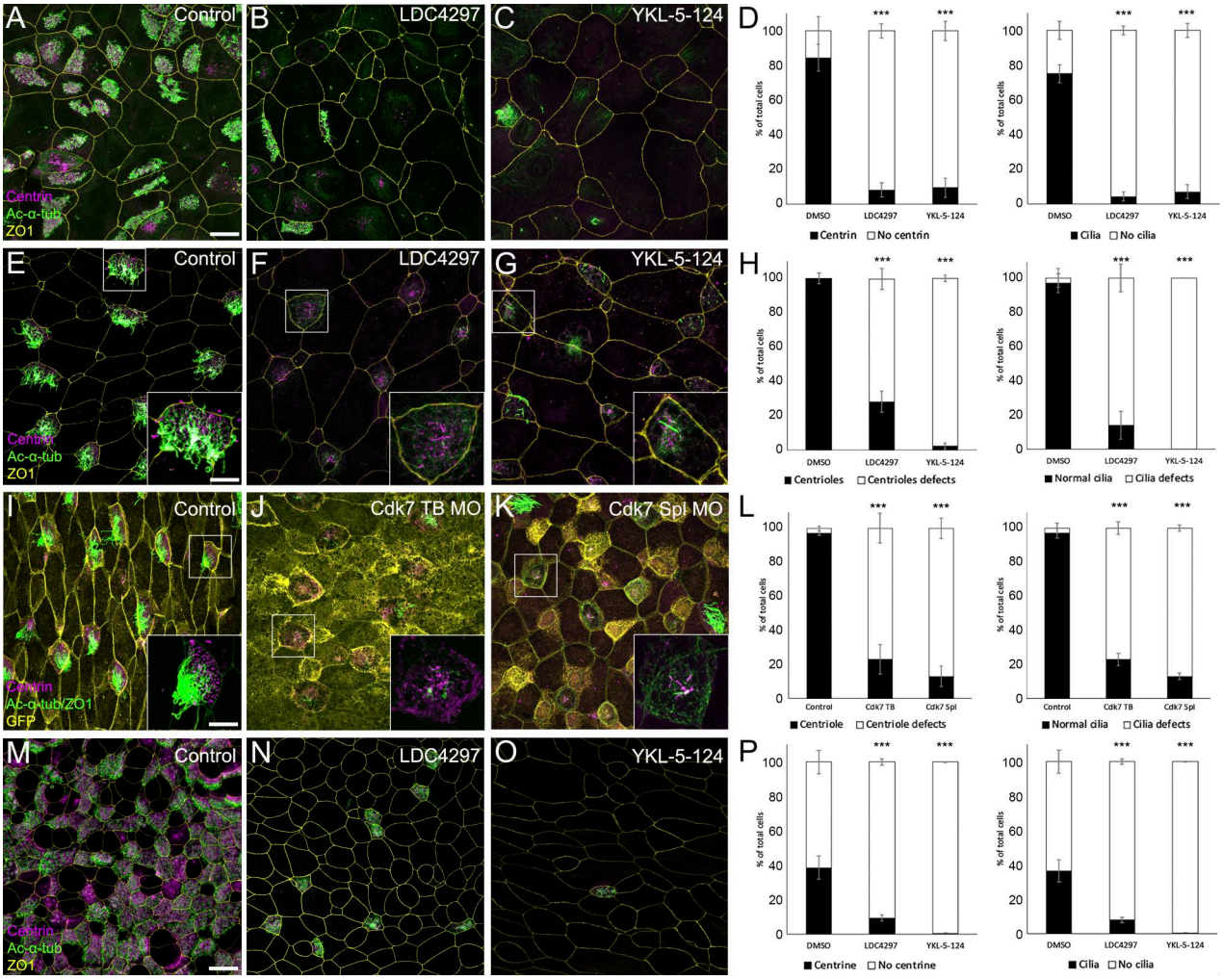

Figure 6. **CDK7 plays a conserved role in differentiating MCCs. (A–C)** Confocal pictures of A6-MCI cells treated with DMSO (control, A) or with CDK7 inhibitors (B and C) and stained for Ac-α-Tub (cilia), centrin (centrioles), and ZO1 (tight junctions). **(D)** Graphs displaying the percentage of cells with or without centriole staining and the percentage of cells with or without cilia staining. *n* = 521 (DMSO), 526 (LDC4297), and 809 (YKL-5-124) cells. SEM is shown. Data were collected from three independent experiments. Fisher's exact test: P <2.2e−16 (***) for LDC4297 and YKL-5-124 vs DMSO. **(E–G)** Confocal pictures of epidermis from *Xenopus* embryos treated with DMSO (control, E) or with CDK7 inhibitors (F and G) and stained for Ac-α-Tub, centrin, and ZO1. **(H)** Graphs displaying the percentage of cells presenting defects in centrioles or cilia. *n* = 341 (DMSO), 337 (LDC4297), and 368 (YKL-5-124) cells. SEM is shown. Data were collected from three independent experiments. Fisher's exact test: P < 2.2e−16 (***) for LDC4297 and YKL-5-124 vs DMSO. **(I–K)** Confocal pictures of epidermis from *Xenopus* embryos injected with GFP (control, I), Cdk7 translation- (TB MO, J), or splice- (Spl MO, K) blocking morpholinos and stained for Ac-α-Tub, centrin, and ZO1. **(L)** Graphs displaying the percentage of cells presenting defects in centrioles or cilia. *n* = 699 (GFP), 826 (Cdk7 TB MO), and 673 (Cdk7 Spl MO) cells. SEM is shown. Data were collected from 15 embryos from three independent experiments. Fisher's exact test: P < 2.2e−16 (***) for MO TB and MO Spl vs control. **(M–O)** Confocal pictures of hAECs treated with DMSO (control, M) or with CDK7 inhibitors (N and O) and stained for Ac-α-Tub, centrin and ZO1. **(P)** Graphs displaying the percentage of cells with or without centriole staining and the percentage of cells with or without cilia staining. *n* = 1551 (DMSO), 732 (LDC4297), and 578 (YKL-5-124) cells. Data were collected from three independent experiments. Fisher's exact test: P < 2.2e−16 (***) for LDC4297 and YKL-5-124 vs DMSO. Scale bar: 15 µm (A–C, E–G, I–K, and M–O).

with 2–3 procentrioles. The major and striking difference with other types of deuterosomal structures is that individual spheres are most often organized in chains of variable length, which can intersect and form larger globular structures. It is important to stress that those observations were made with a specific antibody against *Xenopus* Deup1, which ensured that we detected native deuterosomes. In contrast, approaches based on fusion protein expression may be difficult to interpret due to uncontrolled self-aggregation, which has been reported for Deup1 (Yamamoto et al., 2021). Our observations match those of Steinman on *Xenopus* tracheal and epidermal MCCs, made by TEM over 50 years ago, who reported a linear organization of the core deuterosomal material, which he then called the "procentriole organizer" (Steinman 1968). A first intriguing question emerging from these observations is what causes deuterosomes to adopt different forms? A possible explanation would be that variation in the molecular composition of deuterosomes between different MCC subtypes and/or species could account for variable organizations. The availability of the A6-MCI resource opens the possibility to decipher the *Xenopus* deuterosomal proteome,

thus providing a reference dataset to start answering this question. A second open question relates to the possible link between architecture and the function of deuterosomes. It is clear that MCC subtypes present different characteristics, regarding both the number of cilia produced and their spatial organization (Boutin and Kodjabachian, 2019; Mahjoub et al., 2022). In the future, it would be interesting to investigate whether deuterosome organization influences these parameters.

While A6-MCI cells recapitulate correctly MCC differentiation from the amplification of centrioles around deuterosomes, until their maturation and docking in cytoskeleton networks, we noted defects in the final stages. First, the basal bodies of A6-MCI cells do not coordinate their orientation, as they normally do in natural MCCs. This may be due to the fact that A6-MCI cells lack global polarization information, which *in vivo* is provided by the sequential and combined action of mechanical strain and planar cell polarity proteins (Boutin et al., 2014; Chien et al., 2018). Second, we did not detect fluid flow at the surface of A6-MCI cells, indicating that cilia are unable to undergo synchronous beating. Imperfect MCC differentiation in response to forced MCI expression could reflect the lack of temporal control over MCI activity. Expression data on the *Xenopus* embryo reveal that in epidermal MCCs, *mcidas* transcripts are detected at the time of centriole synthesis but become undetectable when ciliogenesis is engaged (Briggs et al., 2018; Stubbs et al., 2012). This suggests that both the level and timing of MCI activity are critical for the smooth progression into mature MCCs. In A6-MCI cells, the expression *xMCIDAS-hGR* is constitutive, and it is the presence of the ligand-binding domain of the human glucocorticoid receptor that allows the control of the onset of differentiation. However, unlike what happens in natural MCCs, there is no control over the duration of action of MCI once it has translocated into the nucleus. Thus, prolonged MCI activity may interfere with the proper deployment of the motile ciliogenesis gene regulatory network, impeding differentiation into fully functional MCCs. Consistent with this view, we observed that MCCs induced by forced expression of MCI in *Xenopus* epidermis did not display ciliary beating (Video 2).

During MCC differentiation, MCI acts upstream of a gene regulatory network that controls the exit from the cell cycle and the amplification of centrioles (Ma et al., 2014; Stubbs et al., 2012). It also activates FoxJ1, which is responsible for the transcriptional activation of the motile ciliogenesis program (Thomas et al., 2010). MCI is therefore a master regulator, which proved sufficient to induce MCC differentiation from heterologous cell types in the *Xenopus* epidermis (Stubbs et al., 2012). However, not all cells react to MCI expression in the same way. Here, we have shown that RPE1 and Hela cells do not initiate differentiation following MCI expression. Similarly, expression of MCI alone in mouse embryonic fibroblasts only induces centriole overduplication, and co-expression with a constitutively active form of E2F4 is required to activate massive centriole amplification and ciliogenesis (Kim et al., 2018). Thus, it is likely that the identity and/or the epigenetic state preexisting to forced MCI expression impact the capacity for trans-differentiation into MCC.

The A6-MCI culture model is unique and provides significant advantages over other *in vitro* models, such as primary culture of mouse ependymal or tracheal cells. In these models, the differentiation of MCC usually takes several days to weeks and requires specific approaches to remove cells that are not of the MCC lineage or to induce differentiation with ALI. These characteristics are not suitable for large-scale production of biological samples needed for in-depth proteomic approaches. In contrast, the A6-MCI model is highly suitable for these approaches: the culture develops rapidly, is fairly homogeneous, and is easy to handle and to scale up, since it can be grown in simple culture flasks or dishes. These assets have enabled us to produce the quantity of material required for the identification of the global proteome over MCC differentiation. The proteome dataset reflects the synchronicity and homogeneity of the A6-MCI culture across time, which represents an asset compared with the *Xenopus* embryo, for which proteomic experiments are global and may not allow the analysis of rare or modestly abundant cell types, like MCCs that account for only 10% of the total cell pool in the developing epidermis (Walentek, 2018).

The analysis of the MCC proteome allowed the identification of several kinases, which may fuel investigations into the MCC alternative cell cycle, a fundamental concept that has recently emerged in the field (Al Jord et al., 2017; Choksi et al., 2024; Serizay et al., 2025). A first interesting candidate for future functional studies is AurkA. AurkA and PLK1 cooperate to regulate different aspects of the mitotic cycle, including centriole maturation and their disjunction in G2 (Joukov and De Nicolo, 2018). In MCCs, we have implicated PLK1 in the disengagement of neo-synthetized centrioles from deuterosomes (Revinski et al., 2018). Interestingly, both PLK1 and AurkA levels were found to increase between 16 and 24 h before decreasing between 24 and 48 h, suggesting a potential cooperation in terminating the phase of centriole biogenesis. It will be interesting to further probe the implication of AurkA in this context. 9 Cdks were detected in the A6-MCI proteome. Some are dynamically expressed, while others are stably expressed during differentiation. Among them, we further tested the involvement of Cdk7 and showed that inhibition of this kinase at the time of induction prevents the differentiation of A6-MCI cells into MCCs. During the canonical cell cycle, CDK7 plays an instrumental role by phosphorylating CDK1, CDK2, and CDK4/6 (Fisher, 2005). As the latter have all been implicated in the alternative cycle of MCCs (Al Jord et al., 2017; Choksi et al., 2024; Vladar et al., 2018), it is tempting to speculate that they may also be regulated by CDK7 in MCCs. The A6-MCI model is well suited for phosphoproteomic approaches, which could help address this hypothesis. In addition, beyond its role as a regulator of mitotic phases, CDK7 belongs to the family of so-called transcriptional CDKs involved in the regulation of RNA transcription (Fisher, 2005). As such, it would be interesting to investigate possible variations in transcription in the presence or absence of CDK7 activity. As Cdk7 is the first kinase of this type to be involved in the molecular regulation of MCCs, it represents an attractive paradigm to investigate in more detail how transcriptional and posttranslational regulation cooperate to control MCC differentiation.

Broadening our analysis of CDK7, we have shown that its role is not limited to A6-MCI but is conserved in the MCCs of *Xenopus* epidermis, as well as in hAECs. We thus demonstrate that the A6-MCI model has a strong predictive value for understanding the mechanisms at play *in vivo* and in human MCCs. As such, it may help identify factors relevant in the context of ciliopathies. Of note, CDK7 is a promising target in cancer treatment, and several specific inhibitors, including those used in the present study, have entered the clinical development phase (Sava et al., 2020). Here, we show that CDK7 is involved in the development of MCCs, which in humans is a lifelong process that could potentially be affected by CDK7 inhibitor treatments. Our model therefore has implications in cancerology, as it could reveal potential side effects of anticancer therapies.

Materials and methods

Cells and transfection

A6 *Xenopus* cells were obtained from the American Type Culture Collection (ATCC-CCL-A02) and grown at 27°C in complete medium composed of 55% Leibovitz's L15 medium, 10% heat-inactivated FBS, 20 µ/ml penicillin, and 20 µg/ml streptomycin (Thermo Fisher Scientific Bioscience). Cells were transfected with Fugene HD (Ref: E2311; Promega) according to the instructions of the manufacturer. Cells were grown in the presence of 1.5 mg/ml G418 for selection and subsequently 0.5 mg/ml for maintenance.

Plasmids

A pCS2+ plasmid coding for xMCIDAS-hGR (Stubbs et al., 2012) was obtained from Chris Kintner and modified by the insertion of a loxP-flanked Neor cassette (Arakawa et al., 2001) at NotI/KpnI sites. An expression vector coding for Myc-tagged mouse MCIDAS (plentiPGK-Myc-Mcidas) was obtained from Eszter Vladar.

Induction of A6-MCI differentiation and drug treatment

10^6 cells were seeded per well in six-well culture plate and grown at 27°C to confluency in complete G418 medium. The medium was replaced for 24 h with 1% FBS containing medium without G418 and subsequently supplemented with 100 nM (or concentration specified in figures) dexamethasone for additional 24 h or less. Depending on the total incubation time (>24 h), the medium was changed to the same medium without dexamethasone before fixation or lysis. YKL-5-124 and LDC4297, diluted in DMSO at 10 and 2.5 µM, respectively, were added to culture medium either at the time of induction or at different times after induction. Control cells were treated with 0.1% DMSO.

Xenopus embryo culture, drug treatment, and injections

All experiments were performed following the Directive 2010/63/EU of the European parliament and of the council of 22 September, 2010, on the protection of animals used for scientific purposes and approved by the "Direction départementale de la Protection des Populations, Pôle Alimentation, Santé Animale, Environnement, des Bouches du Rhône" (agreement number G 13055 21). Eggs obtained from NASCO females were fertilized *in vitro*, dejellied, and cultured using standard protocols (Revinski et al., 2018). At stage 12, the vitelline membrane was removed from the embryo, and 400 µM of LDC4297 or 200 µM of YKL-5-124 diluted in DMSO was added to the culture medium. Control embryos were treated with 0.4% DMSO. Embryos were incubated at 18°C until they reached stage 27–30. For antibody validation, Deup1 translation (MO1: 5′-GGCTTTCAGTGTCTGTTTGCATTTC-3′ [Mercey et al., 2019]; MO2: 5′-TGTGTCTCCGGCTCCCAGATAAAAC-3′) or splice (MO3: 5′-AAGGAAACAAACCACACTCACCTAC-3′) morpholinos were injected in the 4 blastomeres at NF stage 3. Animal caps from WT embryos or from embryos injected with GFP-GPI (control) or Deup1 MOs were obtained by manual dissection from stage 10 (n = 50 embryos/condition) in 1x MBS and kept in 0.5x MBS until matched control embryos reached stage 18. For Cdk7 knockdown, Cdk7 translation- (Cdk7 TB MO: 5′- CTATACCTTCCATTCTCCCTG-3′; 2.5–3.75 ng/blastomere) or splice- (Cdk7 Spl MO: 5′- CGCAATACAACTCACCTGCC-3′; 30 ng/blastomere) blocking morpholinos were injected in the animal-ventral blastomere at NF stage 4. Embryos were incubated at 18°C until they reached stage 27–30 and were fixed for further analysis. Capped mRNAs were produced using Ambion mMESSAGE mMACHINE kit and purified with Macherey-Nagel NucleoSpin RNA Clean-up kit. To induce MCCs in the epidermis, hGR-MCI (100 pg) and mRFP (200 pg) synthetic mRNAs were co-injected in the animal blastomeres at stage NF stage 2/4. Control embryos were injected with mRFP alone. At stage 10, 5 embryos were treated with 20 µM dexamethasone. Embryos were incubated at 18°C until they reached stage 28 and were mounted between two coverslips for live imaging.

hAECs and drug treatment

Fresh cryopreserved Human Bronchial Epithelial Cells C-12640; PromoCell, Max Passage 3) were thawed in a T75 in Complete PneumaCult-Ex Plus medium and grown in an incubator at 37°C with 5% CO_2. A medium change was performed 24 h after defrosting and every two days until cells reached 50–60% confluence. After trypsinization, 250,000 cells/ml were seeded in Transwells (Corning 6.5-mm Transwell with 0.4-µm Pore polyester Membrane Insert, n°3470, Costar), where both apical and basal chambers were filled with Complete PneumaCult-Ex Plus medium. Just before confluence, cells were placed in ALI by removing medium from the apical chamber and replacing medium in the basal chamber with complete PneumaCult-ALI medium supplemented with 0.25% DMSO (control) or 50 nM LDC4297 or 25 nM YKL-514 diluted in DMSO. Medium change was performed every 2 days, and drug treatments were renewed at the same time. From ALI day 7, dPBS 1X apical washes were performed twice a week to remove excess mucus. From ALI day 23, differentiation of cells was monitored daily using a Nikon Eclipse Ti inverted microscope in bright-field mode. When DMSO controls reached 50% differentiation, cells were fixed in cold methanol at −20°C for 6 min and processed for immunostaining.

Cell lysis and western blotting

Cells were washed in PBS and lysed in 50 mM Tris-HCl, pH 7.5, 150 mM NaCl, and 1 mM EDTA, containing 1% NP-40 and 0.25% sodium deoxycholate (modified RIPA) plus a Complete protease Inhibitor Cocktail (Roche Applied Science) on ice. Cell extracts separated on polyacrylamide gels were transferred onto Optitran membrane (Whatman), followed by incubation with primary antibodies and HRP-conjugated secondary antibodies (Jackson ImmunoResearch Laboratories). Signal obtained from enhanced chemiluminescence (Western Lightning ECL Pro, Perkin Elmer) was detected with MyECL Imager (Thermo Fisher Scientific).

Animal caps were lysed in 200 µl of RIPA buffer (50 mM Tris-HCl, pH 7.5, 150 mM NaCl, 1% NP40, 0.1% SDS, and 0.5% sodium deoxycholate) containing a protease inhibitors tablet (Pierce). Total protein concentration was determined by Bradford assay (Invitrogen), and samples were prepared in LDS sample buffer (Invitrogen) containing a reducing agent. Samples in LDS buffer were denatured for 5 min at 100°C, and 120 µg of proteins were loaded and separated on 4–20% SDS-PAGE (Mini-PROTEAN TGX #456109; Bio-Rad). Following migration, proteins were transferred onto 0.45-µm nitrocellulose membranes (GE Healthcare). Membranes were blocked in TBS for 1 h at RT and then incubated overnight at 4°C with the primary antibody. After three washes in TBS with 0.05% Tween 20 (TBST) buffer for 10 min, the membrane was incubated with the appropriate HRP-conjugated secondary antibody (Peroxidase AffiniPure Donkey Anti-Rabbit IgG (H + L) ref 711-035-152 or Peroxidase AffiniPure Donkey Anti-Mouse IgG (H + L) ref 715-035-151 from Jackson ImmunoResearch) diluted at 1:5000 in TBST-5% dry fat milk, and signals were detected using chemiluminescence.

Generation of *Xenopus* Deup1 antibody

Homemade rabbit antibodies were produced by immunization with recombinant portion of *X. laevis* Deup1 (XP_018103272.1, residues 1–280).

Immunofluorescence staining

A6-MCI cells were grown on glass coverslips and fixed for 6 min in methanol at −20°C. Cells were washed in PBS, blocked in PBS and 3% BSA, and stained with primary antibodies (Table 1) in blocking buffer. After washes in PBS 0.1% Tween-20, cells were incubated with fluorophore-conjugated secondary antibodies (Table 1), washed, and DNA was stained with 250 ng/ml DAPI. Coverslips were then rinsed and mounted in Mowiol.

Xenopus embryos were fixed at RT in PFA and 4–0.1% Triton X-100. Embryos were washed in PBS, blocked in PBS and 3% BSA, and incubated overnight with primary antibodies. After washing in PBS, embryos were incubated for 1 h at RT with fluorophore-conjugated secondary antibodies Table 1 at RT. Embryos were washed with 1X PBS before mounting with Mowiol between slides and coverslips.

hAECs fixed with methanol were washed three times with 1X PBS and 0.1% Tween 20 before blocking in PBS and 3% BSA for 15 min at RT. Cells were incubated for 45 min at RT with primary antibodies (Table 1) diluted in 1X PBS 1X and 3% BSA. After two washes with 1X PBS and 0.1% Tween 20, cells were incubated for 30 min at RT with secondary antibodies (Table 1) diluted in 1X PBS and 3% BSA at RT. After two washes with 1X PBS and 0.1% Tween 20, Transwell membranes were cut before mounting with Mowiol between slides and coverslips.

Antibodies

Table 1. **Antibodies.**

Antibody	Reference	Concentration A6 (expansion)—Xenopus-hAEC
Rabbit anti-myc	Santa Cruz Biotechnology, sc-789	1:500 – /–/
Mouse IgG2a anti-Centrin	Clone 20H5, Merck Millipore, 04-1624	1:1000 (1:500) – 1:1000–1:1000
Mouse IgG2b anti-acetylated α-tubulin	Clone 6-11B-1, Sigma Aldrich, T7451	1:1000 – 1:1000 – 1:1000
Rabbit anti-ZO1	Thermo Fisher Scientific 61-73000	1:200 – /–/
Mouse IgG1 anti-ZO1	Thermo Fisher Scientific 33-9100	1:200 – 1:200 – 1:200
Mouse anti-γ-tubulin	Clone GTU-88, Sigma Aldrich, T5326	1:1000 (1:500) – 1: 800 – /
Rabbit anti-IFT88	Proteintech 13967-1-AP	1:250/–/–/
Rabbit anti-Ruvb2	Abcam ab91462	1:250 – /–/
Rabbit anti-Cep164	Kind gift from Kunsoo Rhee Lab (Seoul); (Kim et al., 2022)	1:800 (1:400) – 1:800 – /
Rabbit anti-Pericentrin	(Nommick et al., 2022)	1:800 – /–/
Rabbit anti-Deup1	This study	1:800 (1:500) – 1:800 – /
Mouse IgG1 anti-β-tubulin	Clone E7, DSHB	1:200 – /–/
Mouse IgG1 anti-Actin	Clone C4, MPBio	1:200 – /–/
DK-anti Rabbit A488	Invitrogen A-21206	1:800 – 1:800 – 1:800
G-anti mIgG2a A568	Invitrogen A-21131	1:800 – 1:800 – 1:800
G-anti mIgG1 A647	Invitrogen A-21240	1:800 – 1:800 – 1:800
G-anti mIgG2b A568	Invitrogen A-21144	1:800 – 1:800 – 1:800
G-anti mIgG2b A488	Invitrogen A-21141	1:800 – 1:800 – 1:800

Expansion microscopy

A6-MCI cells were grown on glass coverslips and fixed for 6 min in MetOH before U-ExM processing according to published protocols (Gambarotto et al., 2019). Briefly, cells were incubated for 5 h in 1.4% formaldehyde (FA)/2% acrylamide (AA) at 37°C. FA/AA solution was removed and replaced by a gelation solution

composed of a monomer solution containing 19% (wt/wt) SA, 10% (wt/wt) AA, and 0.1% (wt/wt) BIS in 1 × PBS supplemented with 0.5% APS and 0.5% TEMED. The gelation step lasted for 5 min on ice and 1 h at 37°C. Coverslips with gel were transferred to a 6-well plate with denaturation buffer (200 mM SDS, 200 mM NaCl, and 50 mM Tris in ultrapure water, pH 9) for 15 min at RT. Gels were transferred to fresh denaturation buffer in 1.5-ml Eppendorf and incubated at 95°C for 30 min. After denaturation, gels were placed in beakers filled with ddH2O for the first expansion. Water was exchanged at least twice every 30 min at RT, and then gels were incubated overnight in ddH2O. Gels were incubated in 1X PBS two times for 15 min before blocking in PBS and 3% BSA for 3 h at 37°C. Primary antibodies (see table below) diluted in PBS and 2% BSA were added for 3 h at 37°C. After washing with PBST three times for 10 min, gels were incubated with secondary antibodies (see table below) diluted in PBS and 3% BSA for 3 h at 37°C. Gels were washed three times for 10 min under agitation and placed in ddH2O for final expansion. ddH2O was exchanged at least twice every 30 min, and gels were incubated in ddH2O overnight. Gels expanded around fourfold.

Imaging and quantification

Confocal images were acquired by capturing Z-series with 0.3-µm step size using an LSM 780 or 880 (Zeiss) or SP8 (Leica microsystems) laser scanning microscope equipped with 63X Oil, 1.4 NA objectives. Images were converted into single-plane maximum intensity projection and processed using Fiji software. STED super-resolution images were acquired with a TCS SP8 STED 3X microscope equipped with an HC PL APO 93X/1.30 GLYC motCORRTM objective (Leica microsystems). Movies of ciliary beating were acquired using an LSM 880. For each movie, Z confocal time series were acquired every 3 s. Circular SD quantifications were done using the BioTool software (Boutin et al., 2014).

Prism, Excel, and R studio software were used for graphical representations and statistical analysis. The following statistical tests were applied: Fig. 3: Unpaired *t* test with Welch's correction (two-tailed); Figs. 6 and S5: Fisher's exact test (one-tailed).

The average maps of Fig. 3 D were obtained through the following three steps: manual picking in the confocal data (Fig. 3 C) of 36 particles for centrin/Cep164 labelling and 14 particles for gamma-tubulin/Cep164 labelling; reference-free reconstruction of a coarse average map using the method described in (Eloy et al., 2023); refinement of this initial map using the approach detailed in (Fortun et al., 2016). A C9 symmetry constraint was imposed to all reconstructions except for the gamma-tubulin channel. All these steps were performed with the publicly available SP-Fluo software (https://spfluo.icube.unistra.fr/en/usage/installation.html).

Flow analysis on A6-MCI and embryos

Tadpoles were kept in anesthetic (0.02% MS-222 in 0.1X MBS) lying on their sides. 10-µm fluorescent beads (Invitrogen) were then released near the top of embryos heads or on top of mature A6-MCI culture using a 2-µl Hamilton syringe. Videos (20 frames per seconds) were recorded at 3× magnification using a Fluorescence stereomicroscope (Nikon SMZ18) coupled with a digital camera (Hamamatsu ORCA-fusion C14440) using 10 ms exposure.

TEM, tomography, and segmentation

Cells were fixed with 2.5% glutaraldehyde and 2% PFA 0.1 M in cacodylate buffer, pH 7.4, and post-fixed with 1% osmium tetroxide in 0.1 M cacodylate buffer, pH 7.4, for 1 h at RT. They were dehydrated in alcohol and embedded in Epon. Next, cells were cut transversely (70 nm/slice for serial sections 300 nm/slice for tomograms) with a Leica Ultracut UC7 (Leica, Germany), and the serial sections were collected on grids. To observe and reconstruct entire deuterosomes, images or tomograms were acquired on several consecutive sections until no deuterosomal material was visible on the edge sections. Images were acquired using a Tecnai G2 (Thermo Fisher Scientific) microscope, running an LaB6 crystal at 200 kV and equipped with a 2K Veleta camera (Olympus, Japan). For tomograms, dual-axis tilt series were acquired at 62 kx (0.94 nm/px) or 80 kx (0.73 nm/px) following the Saxton scheme (0° tilt step: 1°) from −60° to +60°.

Tomographic reconstructions were carried out in IMOD, using cross-correlation for tilt series alignment and a back projection algorithm for reconstruction. The IMOD MIDAS semiautomated alignment tool was used to join serial tomograms.

The reconstructed volumes were denoised by the anisotropic diffusion filter in Amira and treated with the FeatureJ plugin in Fiji before segmentation by pixel classification in ilastik. Probability maps of segmentation were imported into Dragonfly, where the core versus the centriolar material were discriminated using the multi-slice brush tool in adaptive Gaussian mode. Segmented volumes were finally exported to Amira for movie generation.

Samples collection for proteomic analysis

For each condition, 2 × 10^7 cells were seeded in 10-cm culture dish and grown at 27°C to confluency in complete G418 medium. The medium was replaced for 24 h with 1% FBS-containing medium without G418 before induction with 100 nM dexamethasone. Cells were washed twice with cold 1X PBS and incubated for 4 min in RIPA lysis buffer complemented with protease and phosphatase inhibitor (#78441; Thermo Fisher Scientific). Cell lysate was collected, incubated for 15 min on ice with nuclease (#88700; Thermo Fisher Scientific), and centrifuged for 25 min at 16000 *g* at 4°C. Cell extracts were collected, proteins were measured using a BCA kit, and samples were adjusted to a concentration of 2 mg/ml in RIPA buffer.

Mass spectrometry

15 µg of protein samples was prepared in LDS buffer and proteins extract were loaded on NuPAGE 4–12% bis–Tris AA gels according to the manufacturer's instructions (Life Technologies). Running of protein was stopped as soon as proteins stacked in a single band. Protein containing bands were stained with Imperial Blue (Pierce), cut from the gel, and digested with high-sequencing grade trypsin (Promega) before mass spectrometry analysis. Gel pieces were washed and destained using few steps of 100 mM NH4HCO3. Destained gel pieces were shrunk with

100 mM ammonium bicarbonate in 50% acetonitrile and dried at RT. Protein spots were then rehydrated using 10 mM DTT in 25 mM ammonium bicarbonate, pH 8.0, for 45 min at 56°C. This solution was replaced by 55 mM iodoacetamide in 25 mM ammonium bicarbonate, pH 8.0, and the gel pieces were incubated for 30 min at RT in the dark. They were then washed twice in 25 mM ammonium bicarbonate and finally shrunk by incubation for 5 min with 25 mM ammonium bicarbonate in 50% acetonitrile. The resulting alkylated gel pieces were dried at RT. The dried gel pieces were reswollen by incubation in 25 mM ammonium bicarbonate, pH 8.0, supplemented with 12.5 ng/µl trypsin (Promega) for 1 h at 4°C and then incubated overnight at 37°C. Peptides were harvested by collecting the initial digestion solution and carrying out two extractions; first in 5% formic acid and then in 5% formic acid in 60% acetonitrile. Pooled extracts were dried down in a centrifugal vacuum system. Samples were reconstituted in 0.1% TFA and 4% acetonitrile before mass spectrometry using an Orbitrap Fusion Lumos Tribrid Mass Spectrometer online with a Vanquish Neo chromatography system (Thermo Fisher Scientific). Peptides were separated at 40°C using a two-step linear gradient (4–20% acetonitrile/H_2O; 0.1% formic acid for 110 min and 20–32% acetonitrile/H_2O; 0.1% formic acid for 10 min). An EASY-Spray nanosource was used for peptide ionization (1,900 V, 275°C). MS was conducted using a data-independent acquisition mode (DIA). Full MS scans were acquired in the range of m/z 375–1,500 at a resolution of 120,000 at m/z 200, and the automatic gain control was set at 4.0 × 10E5 with a 50 -ms maximum injection time. MS2 spectra were acquired in the Orbitrap with a resolution of 30,000, in the mass range of 200–1800 m/z after isolation of parent ion in the quadrupole and fragmentation in the HCD cell under collision energy of 30%. DIA parent ion range was from 400 to 1000 m/z divided into 40 windows 16 Da wide and from 1,000 to 1,500 m/z divided into 10 windows 50 Da wide.

Mass spectrometry data processing

For protein identification and quantification, relative intensity-based label-free quantification (LFQ) was processed using the DIA-NN 1.8 algorithm (Demichev et al., 2020). Raw files were searched against the *X. laevis* UP000186698, extracted from UniProtKB (date 2023-07-23; 35869 entries, OneProteinSeqPerGene) implemented with a contaminant database (Frankenfield et al., 2022). The following parameters were used for searches: (1) trypsin allowing cleavage before proline; (2) one missed cleavage was allowed; (3) cysteine carbamidomethylation (+57.02146) as a fixed modification and methionine oxidation (+15.99491) and N-terminal acetylation (+42.0106) as variable modifications; (4) a maximum of 1 variable modification per peptide was allowed; and (5) minimum peptide length was 7 amino acids and a maximum of 30 amino acids. The match between the runs option was enabled. The precursor false discovery was set to 1%. DIA-NN parameters were set on double-pass mode for Neural Network classifier, Robust LC high precision for quantification strategy, and RT-dependent mode for cross-run normalization. Library was generated using Smart profiling setup. MS1 and MS2 mass accuracy was automatically calculated for precursor charge fixed between 2 and 4. Main output file from DIA-NN was further filtered at 1% FDR, and LFQ intensity was calculated using our DIAgui package at 1% q value (https://github.com/marseille-proteomique/DIAgui [Gerault et al., 2024]). The statistical analysis was done with Perseus software (version 1.6.15.0), where proteins were pre-filtered to remove contaminants (Tyanova and Cox, 2018). Each biological sample was prepared in triplicate; each triplicate was analyzed three times by LC-MS/MS. Relative quantification was calculated using fold changes of LFQ intensity between two conditions. To determine whether a given detected protein was specifically differential, a two-sample *t* test was done using permutation-based FDR-controlled employing 250 permutations. Differential proteins were detected using a two-sample *t* test at 0.05 permutation-based false discovery rate. Statistical analysis was performed using the standard two-tailed Student's *t* test, and P value < 0.05 was considered significant. Volcano plots were created using Prism software. GO analysis was performed using STRING database (Version 12.0).

Online supplemental material

Fig. S1 shows effects of dexamethasone concentration and application time on the differentiation of A6-MCI cells. Fig. S2 shows characterization of the *Xenopus* Deup1 antibody and time course western blot analysis of MCC markers in A6-MCI. Fig. S3 shows immunostaining time course des marques des MCCs dans A6-MCI. Fig. S4 shows STED and TEM analysis of A6-MCI deuterosomes. Fig. S5 shows time course analysis of the effect of CDK7 inhibition on A6-MCI cells and *Xenopus* embryos. Table S1 shows lists of proteins differentially expressed during A6-MCI cell differentiation. Video 1 shows analysis of flow in A6-MCI culture. Video 2 shows ciliary beating in WT and MCI-injected *Xenopus* embryos. Video 3 shows tomogram and 3D reconstruction of a short deuterosome. Video 4 shows tomogram and 3D tomogram reconstruction of a long deuterosome chain. Video 5 shows tomogram and 3D reconstruction of a ramified deuterosome chain.

Data availability

The data underlying Figs. 1, 2, 3, 4, 5, S1, S2, S3, S4, and S5 are available in the published article and its online supplemental material. Proteomic data have been deposited to the ProteomeXchange Consortium via the PRIDE partner repository (Perez-Riverol et al., 2025) with the dataset identifier PXD064476.

Acknowledgments

We thank Emmanuelle Leblanc and Florian Roguet for *Xenopus* husbandry. J.-P. Borg is a scholar of the Institut Universitaire de France. We thank Julia Schaeffer and Peter Walentek for insightful comments on the manuscript.

This work received support from the French government under the France 2030 investment plan, as part of the Initiative d'Excellence d'Aix-Marseille Université – A*MIDEX" AMX-21-PEP-042 ('Pépinière d'Excellence 2021 to C. Boutin), Cancéropôle PACA-GEFLUC (Programme Emergence 2021 to C.

Boutin), and ANR (ANR-22-CE13-0027 PHACIL to C. Boutin, ANR-19-CE13-0033 MCCproteome to L. Kodjabachian and J.-P. Borg, and ANR20-CE45-0007 SP-Fluo to D. Fortun). Imaging was performed at IBDM, a member of the National Infrastructure France-BioImaging (https://ror.org/01y7vt929) supported by the French National Research Agency (ANR-24-INBS-0005 FBI BIOGEN). The mass spectrometry facility of Marseille Proteomics (https://marseille-proteomique.univ-amu.fr/) is supported by Infrastructures en Biologie Santé et Agronomie, the Cancéropôle PACA, the Région Sud, the Institut Paoli-Calmettes, and Fonds Européen de Développement Régional.

Author contributions: Camille Boutin: conceptualization, formal analysis, funding acquisition, investigation, methodology, project administration, supervision, validation, visualization, and writing—original draft, review, and editing. Olivier Rosnet: investigation, methodology, resources, visualization, and writing—review and editing. Marine Touret: formal analysis, investigation, and writing—review and editing. Stephane Audebert: conceptualization, formal analysis, investigation, methodology, resources, and visualization. Luc Camoin: formal analysis, investigation, and methodology. Salome Dussert: methodology and writing—review and editing. Nicolas Brouilly: investigation, methodology, and writing—review and editing. Virginie Thome: investigation. Jean Plumail: software and visualization. Denis Fortun: formal analysis and software. Jean-Paul Borg: supervision. Laurent Kodjabachian: conceptualization, funding acquisition, resources, and writing—review, and editing.

Disclosures: The authors declare no competing interests exist.

Submitted: 23 June 2025
Revised: 8 December 2025
Accepted: 5 January 2026

References

Al Jord, A., A.I. Lemaitre, N. Delgehyr, M. Faucourt, N. Spassky, and A. Meunier. 2014. Centriole amplification by mother and daughter centrioles differs in multiciliated cells. *Nature*. 516:104–107. https://doi.org/10.1038/nature13770

Al Jord, A., A. Shihavuddin, R. Servignat d'Aout, M. Faucourt, A. Genovesio, A. Karaiskou, J. Sobczak-Thepot, N. Spassky, and A. Meunier. 2017. Calibrated mitotic oscillator drives motile ciliogenesis. *Science*. 358: 803–806. https://doi.org/10.1126/science.aan8311

Anderson, R.G., and R.M. Brenner. 1971. The formation of basal bodies (centrioles) in the Rhesus monkey oviduct. *J. Cell Biol*. 50:10–34. https://doi.org/10.1083/jcb.50.1.10

Arakawa, H., D. Lodygin, and J.M. Buerstedde. 2001. Mutant loxP vectors for selectable marker recycle and conditional knock-outs. *BMC Biotechnol*. 1: 7. https://doi.org/10.1186/1472-6750-1-7

Boutin, C., and L. Kodjabachian. 2019. Biology of multiciliated cells. *Curr. Opin. Genet. Dev*. 56:1–7. https://doi.org/10.1016/j.gde.2019.04.006

Boutin, C., P. Labedan, J. Dimidschstein, F. Richard, H. Cremer, P. Andre, Y. Yang, M. Montcouquiol, A.M. Goffinet, and F. Tissir. 2014. A dual role for planar cell polarity genes in ciliated cells. *Proc. Natl. Acad. Sci. USA*. 111:E3129–E3138. https://doi.org/10.1073/pnas.1404988111

Brenner, R.M. 1969. Renewal of oviduct cilia during the menstrual cycle of the rhesus monkey. *Fertil. Steril*. 20:599–611. https://doi.org/10.1016/s0015-0282(16)37086-8

Briggs, J.A., C. Weinreb, D.E. Wagner, S. Megason, L. Peshkin, M.W. Kirschner, and A.M. Klein. 2018. The dynamics of gene expression in vertebrate embryogenesis at single-cell resolution. *Science*. 360: eaar5780. https://doi.org/10.1126/science.aar5780

Chien, Y.H., S. Srinivasan, R. Keller, and C. Kintner. 2018. Mechanical strain determines cilia length, motility, and planar position in the left-right organizer. *Dev. Cell*. 45:316–330.e4. https://doi.org/10.1016/j.devcel.2018.04.007

Choksi, S.P., L.E. Byrnes, M.J. Konjikusic, B.W.H. Tsai, R. Deleon, Q. Lu, C.J. Westlake, and J.F. Reiter. 2024. An alternative cell cycle coordinates multiciliated cell differentiation. *Nature*. 630:214–221. https://doi.org/10.1038/s41586-024-07476-z

Demichev, V., C.B. Messner, S.I. Vernardis, K.S. Lilley, and M. Ralser. 2020. DIA-NN: Neural networks and interference correction enable deep proteome coverage in high throughput. *Nat. Methods*. 17:41–44. https://doi.org/10.1038/s41592-019-0638-x

Eloy, T., E. Baudrier, M. Laporte, V. Hamel, P. Guichard, and D. Fortun. 2023. Fast and robust single particle reconstruction in 3D fluorescence microscopy. *IEEE Trans. Comput. Imaging*. 636:648–649.

Fisher, R.P. 2005. Secrets of a double agent: CDK7 in cell-cycle control and transcription. *J. Cell Sci*. 118:5171–5180. https://doi.org/10.1242/jcs.02718

Fortun, D., P. Guichard, N. Chu, and M. Unser. 2016. Reconstruction from multiple poses in fluorescence imaging: Proof of concept. *IEEE J. Selected Top. Signal Process*. 61:70–100.

Frankenfield, Ashley M, Jiawei Ni, Mustafa Ahmed, and Ling Hao. 2022. Protein Contaminants Matter: Building Universal Protein Contaminant Libraries for DDA and DIA Proteomics. *J Proteome Res*. 21(9):2104–2113. https://doi.org/10.1021/acs.jproteome.2c00145

Gambarotto, D., F.U. Zwettler, M. Le Guennec, M. Schmidt-Cernohorska, D. Fortun, S. Borgers, J. Heine, J.G. Schloetel, M. Reuss, M. Unser, et al. 2019. Imaging cellular ultrastructures using expansion microscopy (U-ExM). *Nat. Methods*. 16:71–74. https://doi.org/10.1038/s41592-018-0238-1

Gerault, M.A., L. Camoin, and S. Granjeaud. 2024. DIAgui: A shiny application to process the output from DIA-NN. *Bioinform Adv*. 4:vbae001. https://doi.org/10.1093/bioadv/vbae001

Huizar, R.L., C. Lee, A.A. Boulgakov, A. Horani, F. Tu, E.M. Marcotte, S.L. Brody, and J.B. Wallingford. 2018. A liquid-like organelle at the root of motile ciliopathy. *Elife*. 7:e38497. https://doi.org/10.7554/eLife.38497

Joukov, V., and A. De Nicolo. 2018. Aurora-PLK1 cascades as key signaling modules in the regulation of mitosis. *Sci. Signal*. 11:eaar4195. https://doi.org/10.1126/scisignal.aar4195

Kalnins, V.I., and K.R. Porter. 1969. Centriole replication during ciliogenesis in the chick tracheal epithelium. *Z. Zellforsch Mikrosk Anat*. 100:1–30. https://doi.org/10.1007/BF00343818

Kim, S., L. Ma, M.N. Shokhirev, I. Quigley, and C. Kintner. 2018. Multicilin and activated E2f4 induce multiciliated cell differentiation in primary fibroblasts. *Sci. Rep*. 8:12369. https://doi.org/10.1038/s41598-018-30791-1

Kim, S., Y.H. Chien, A. Ryan, and C. Kintner. 2022. Emi2 enables centriole amplification during multiciliated cell differentiation. *Sci. Adv*. 8: eabm7538. https://doi.org/10.1126/sciadv.abm7538

Klos Dehring, D.A., E.K. Vladar, M.E. Werner, J.W. Mitchell, P. Hwang, and B.J. Mitchell. 2013. Deuterosome-mediated centriole biogenesis. *Dev. Cell*. 27:103–112. https://doi.org/10.1016/j.devcel.2013.08.021

Kyrousi, C., M. Arbi, G.A. Pilz, D.E. Pefani, M.E. Lalioti, J. Ninkovic, M. Gotz, Z. Lygerou, and S. Taraviras. 2015. Mcidas and GemC1 are key regulators for the generation of multiciliated ependymal cells in the adult neurogenic niche. *Development*. 142:3661–3674. https://doi.org/10.1242/dev.126342

Lewis, M., B. Terre, P.A. Knobel, T. Cheng, H. Lu, C.S. Attolini, J. Smak, E. Coyaud, I. Garcia-Cao, S. Sharma, et al. 2023. GEMC1 and MCIDAS interactions with SWI/SNF complexes regulate the multiciliated cell-specific transcriptional program. *Cell Death Dis*. 14:201. https://doi.org/10.1038/s41419-023-05720-4

Ma, L., I. Quigley, H. Omran, and C. Kintner. 2014. Multicilin drives centriole biogenesis via E2f proteins. *Genes Dev*. 28:1461–1471. https://doi.org/10.1101/gad.243832.114

Mahjoub, M.R., R. Nanjundappa, and M.N. Harvey. 2022. Development of a multiciliated cell. *Curr. Opin. Cell Biol*. 77:102105. https://doi.org/10.1016/j.ceb.2022.102105

Mercey, O., M.S. Levine, G.M. LoMastro, P. Rostaing, E. Brotslaw, V. Gomez, A. Kumar, N. Spassky, B.J. Mitchell, A. Meunier, and A.J. Holland. 2019. Massive centriole production can occur in the absence of deuterosomes

in multiciliated cells. *Nat. Cell Biol.* 21:1544–1552. https://doi.org/10.1038/s41556-019-0427-x

Nommick, A., C. Boutin, O. Rosnet, C. Schirmer, E. Bazellieres, V. Thome, E. Loiseau, A. Viallat, and L. Kodjabachian. 2022. Lrrcc1 and Ccdc61 are conserved effectors of multiciliated cell function. *J. Cell Sci.* 135: jcs258960. https://doi.org/10.1242/jcs.258960

Pan, J.H., T.L. Adair-Kirk, A.C. Patel, T. Huang, N.S. Yozamp, J. Xu, E.P. Reddy, D.E. Byers, R.A. Pierce, M.J. Holtzman, and S.L. Brody. 2014. Myb permits multilineage airway epithelial cell differentiation. *Stem Cells*. 32:3245–3256. https://doi.org/10.1002/stem.1814

Perez-Riverol, Y., C. Bandla, D.J. Kundu, S. Kamatchinathan, J. Bai, S. Hewapathirana, N.S. John, A. Prakash, M. Walzer, S. Wang, and J.A. Vizcaino. 2025. The PRIDE database at 20 years: 2025 update. *Nucleic Acids Res.* 53:D543–D553. https://doi.org/10.1093/nar/gkae1011

Quigley, I.K., and C. Kintner. 2017. Rfx2 stabilizes Foxj1 binding at chromatin loops to enable multiciliated cell gene expression. *PLoS Genet.* 13: e1006538. https://doi.org/10.1371/journal.pgen.1006538

Rafferty, K.A., Jr. 1969. Mass culture of amphibian cells: Methods and observations concerning stability of cell type. *In* Biology of Amphibian Tumors. M. Mizell, editor. Springer, New York, NY. 52–81.

Redman, E., M. Fierville, A. Cavard, M. Plaisant, M.J. Arguel, S. Ruiz Garcia, E.M. McAndrew, C. Girard-Riboulleau, K. Lebrigand, V. Magnone, et al. 2024. Cell culture differentiation and proliferation conditions influence the in vitro regeneration of the human airway epithelium. *Am. J. Respir. Cell Mol. Biol.* 71:267–281. https://doi.org/10.1165/rcmb.2023-0356MA

Revinski, D.R., L.E. Zaragosi, C. Boutin, S. Ruiz-Garcia, M. Deprez, V. Thome, O. Rosnet, A.S. Gay, O. Mercey, A. Paquet, et al. 2018. CDC20B is required for deuterosome-mediated centriole production in multiciliated cells. *Nat. Commun.* 9:4668. https://doi.org/10.1038/s41467-018-06768-z

Sava, G.P., H. Fan, R.C. Coombes, L. Buluwela, and S. Ali. 2020. CDK7 inhibitors as anticancer drugs. *Cancer Metastasis Rev.* 39:805–823. https://doi.org/10.1007/s10555-020-09885-8

Serizay, J., M. Khoury Damaa, A.R. Boudjema, R. Balague, M. Faucourt, N. Delgehyr, C. Nous, L.E. Zaragosi, P. Barbry, N. Spassky, et al. 2025. Cyclin switch tailors a cell cycle variant to orchestrate multiciliogenesis. *Cell Rep.* 44:115103. https://doi.org/10.1016/j.celrep.2025.116523

Sorokin, S.P. 1968. Reconstructions of centriole formation and ciliogenesis in mammalian lungs. *J. Cell Sci.* 3:207–230. https://doi.org/10.1242/jcs.3.2.207

Spassky, N., and A. Meunier. 2017. The development and functions of multiciliated epithelia. *Nat. Rev. Mol. Cell Biol.* 18:423–436. https://doi.org/10.1038/nrm.2017.21

Steinman, R.M. 1968. An electron microscopic study of ciliogenesis in developing epidermis and trachea in the embryo of Xenopus laevis. *Am. J. Anat.* 122:19–55. https://doi.org/10.1002/aja.1001220103

Stubbs, J.L., E.K. Vladar, J.D. Axelrod, and C. Kintner. 2012. Multicilin promotes centriole assembly and ciliogenesis during multiciliate cell differentiation. *Nat. Cell Biol.* 14:140–147. https://doi.org/10.1038/ncb2406

Tan, F.E., E.K. Vladar, L. Ma, L.C. Fuentealba, R. Hoh, F.H. Espinoza, J.D. Axelrod, A. Alvarez-Buylla, T. Stearns, C. Kintner, and M.A. Krasnow. 2013. Myb promotes centriole amplification and later steps of the multiciliogenesis program. *Development*. 140:4277–4286. https://doi.org/10.1242/dev.094102

Thomas, J., L. Morle, F. Soulavie, A. Laurencon, S. Sagnol, and B. Durand. 2010. Transcriptional control of genes involved in ciliogenesis: A first step in making cilia. *Biol. Cell*. 102:499–513. https://doi.org/10.1042/BC20100035

Tyanova, S., and J. Cox. 2018. Perseus: A bioinformatics platform for integrative analysis of proteomics data in cancer research. *Methods Mol. Biol.* 1711:133–148. https://doi.org/10.1007/978-1-4939-7493-1_7

Vladar, E.K., M.B. Stratton, M.L. Saal, G. Salazar-De Simone, X. Wang, D. Wolgemuth, T. Stearns, and J.D. Axelrod. 2018. Cyclin-dependent kinase control of motile ciliogenesis. *Elife*. 7:e36375. https://doi.org/10.7554/eLife.36375

Walentek, P. 2018. Manipulating and analyzing cell type composition of the Xenopus mucociliary epidermis. *Methods Mol. Biol.* 1865: 251–263. https://doi.org/10.1007/978-1-4939-8784-9_18

Wallmeier, J., K.G. Nielsen, C.E. Kuehni, J.S. Lucas, M.W. Leigh, M.A. Zariwala, and H. Omran. 2020. Motile ciliopathies. *Nat. Rev. Dis. Primers*. 6: 77. https://doi.org/10.1038/s41572-020-0209-6

Werner, M.E., P. Hwang, F. Huisman, P. Taborek, C.C. Yu, and B.J. Mitchell. 2011. Actin and microtubules drive differential aspects of planar cell polarity in multiciliated cells. *J. Cell Biol.* 195:19–26. https://doi.org/10.1083/jcb.201106110

Yamamoto, S., R. Yabuki, and D. Kitagawa. 2021. Biophysical and biochemical properties of Deup1 self-assemblies: A potential driver for deuterosome formation during multiciliogenesis. *Biol. Open*. 10:bio056432. https://doi.org/10.1242/bio.056432

Zhao, H., L. Zhu, Y. Zhu, J. Cao, S. Li, Q. Huang, T. Xu, X. Huang, X. Yan, and X. Zhu. 2013. The Cep63 paralogue Deup1 enables massive de novo centriole biogenesis for vertebrate multiciliogenesis. *Nat. Cell Biol.* 15: 1434–1444. https://doi.org/10.1038/ncb2880

Supplemental material

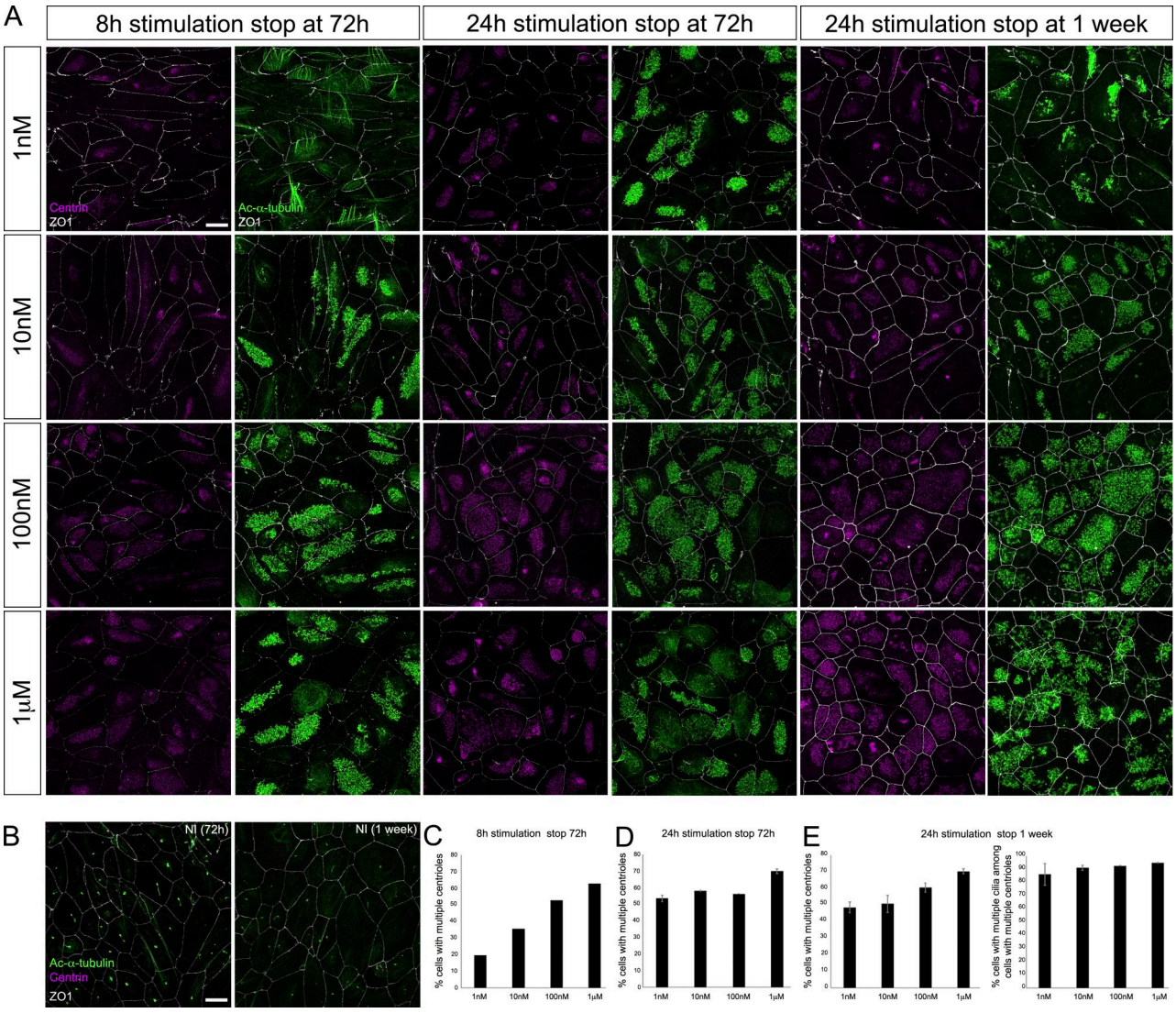

Figure S1. **Effects of dexamethasone concentration and application time on the differentiation of A6-MCI cells. (A)** Confocal pictures of A6-MCI cells induced with variable concentrations of dexamethasone, applied at variable times and cultured for variable durations, as indicated, and stained for centrin (centrioles), Ac-α-Tub (cilia), and ZO1 (tight junctions). **(B)** Confocal pictures of NI A6-MCI cells stained for centrin, Ac-α-Tub and ZO1 after 72 h or 1 week of culture. **(C)** Graph showing the percentage of cells with multiple centrioles at 72 hpi for 8-h stimulation with increasing dexamethasone concentrations. *n* = 287 (1 nM), 418 (10 nM), 501 (100 nM), and 439 (1 µM) cells. SD between field of view is shown. Data were collected from one experiment. **(D)** Graph showing the percentage of cells with multiple centrioles at 72 hpi for 24-h stimulation with increasing dexamethasone concentrations. *n* = 936 (1 nM), 1277 (10 nM), 1432 (100 nM), and 1282 (1 µM) cells. SD between field of view is shown. Data were collected from one experiment. **(E)** Graphs showing the percentage of cells with multiple centrioles and with multiple cilia at 1 wk after induction for 24-h stimulation with increasing dexamethasone concentrations. *n* = 1111 (1 nM), 1253 (10 nM), 1483 (100 nM), and 1379 (1 µM) cells. SDs between experiments are shown. Data were collected from three independent experiments.

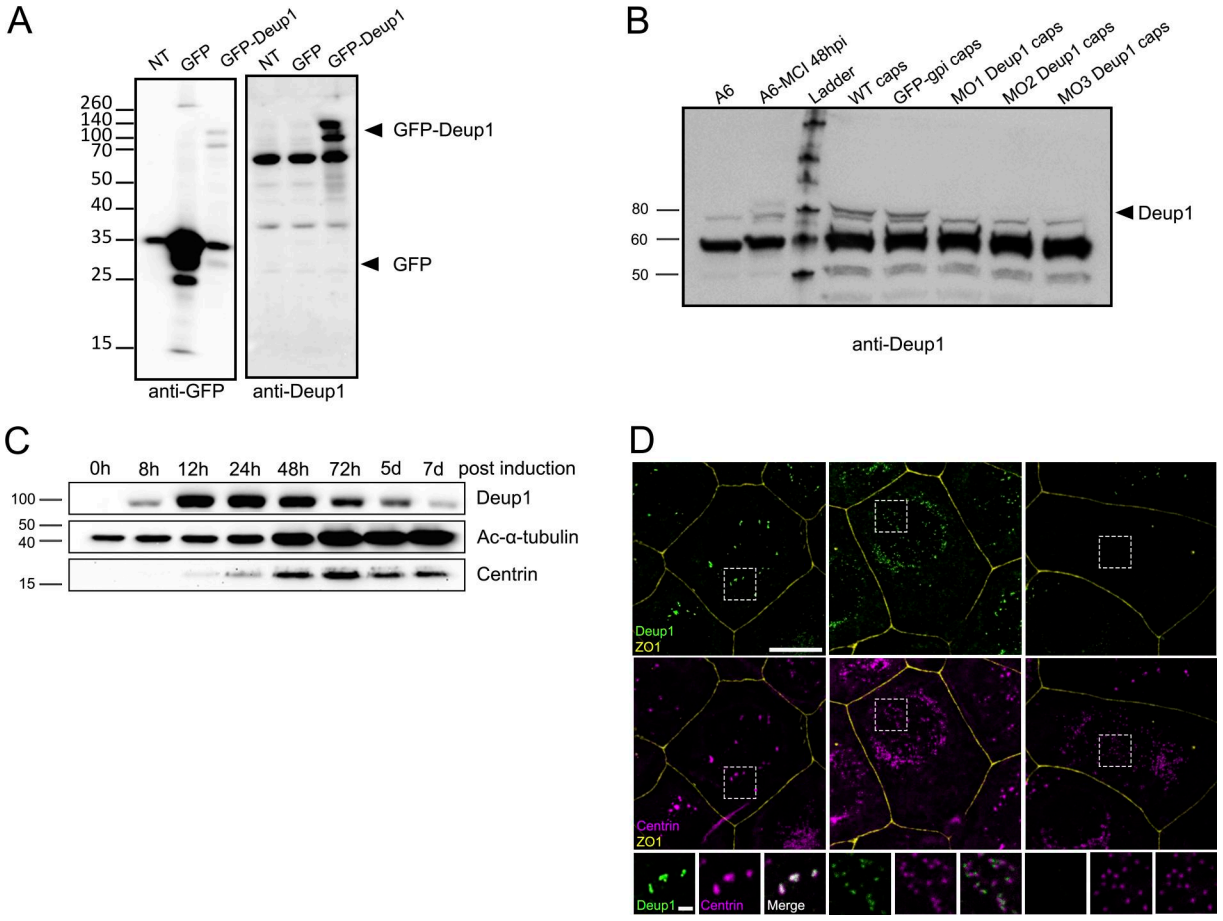

Figure S2. **Characterization of Xenopus Deup1 antibody and time course analyzis of MCCs markers in A6-MCI cells. (A)** Cos1 cells were transfected with the indicated construct and immunoblotted with anti-GFP (left panel) or homemade anti-Deup1 antibody (right panel). **(B)** A6, A6-MCI, or St18 *Xenopus* animal caps injected with the indicated construct, or morpholinos targeting Deup1, were immunoblotted with anti-Deup1 antibody. The Deup1-specific band disappears in animal caps injected with 3 distinct morpholinos against Deup1. **(C)** Western blot showing the expression of Deup1, centrin, and Ac-α-Tub in A6-MCI cells at the indicated times after induction. **(D)** Confocal pictures of A6-MCI cells stained with Deup1, centrin, and ZO1 antibodies reveal A6-MCI differentiation stages. At the stage of centriole production (left), Deup1 and centrin reveal globular structures, which correspond to deuterosomes surrounded by growing centrioles. Later (middle), centrin staining reveals released centrioles associated with Deup1 puncta. In mature cells (right), Deup1 is no longer detectable at apically positioned centrioles. Source data are available for this figure: SourceData FS2. Original Ponceau membrane and gel of data shown in Fig. S1. Ponceau-stained membranes were cut along indicated dotted lines. Membranes were incubated with the indicated antibodies. Red rectangles indicate the regions of the gel that are shown in Fig. S1. Note that colorimetric and chemiluminescent ladders were loaded in the same well in Fig. S2 B.

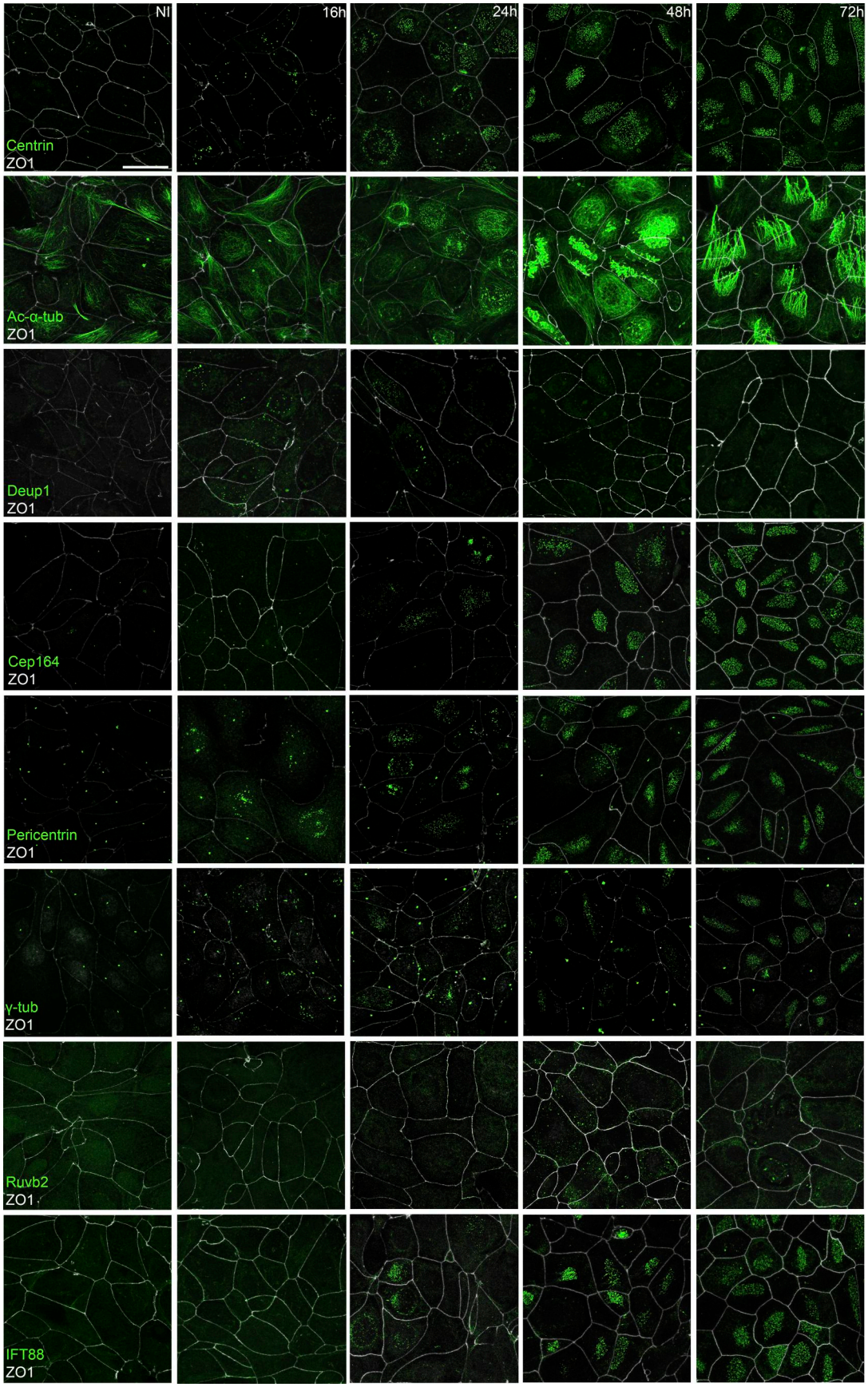

Figure S3. **Confocal pictures of A6-MCI cells at the indicated times after induction and stained with the indicated markers.** Scale bar: 25 µm.

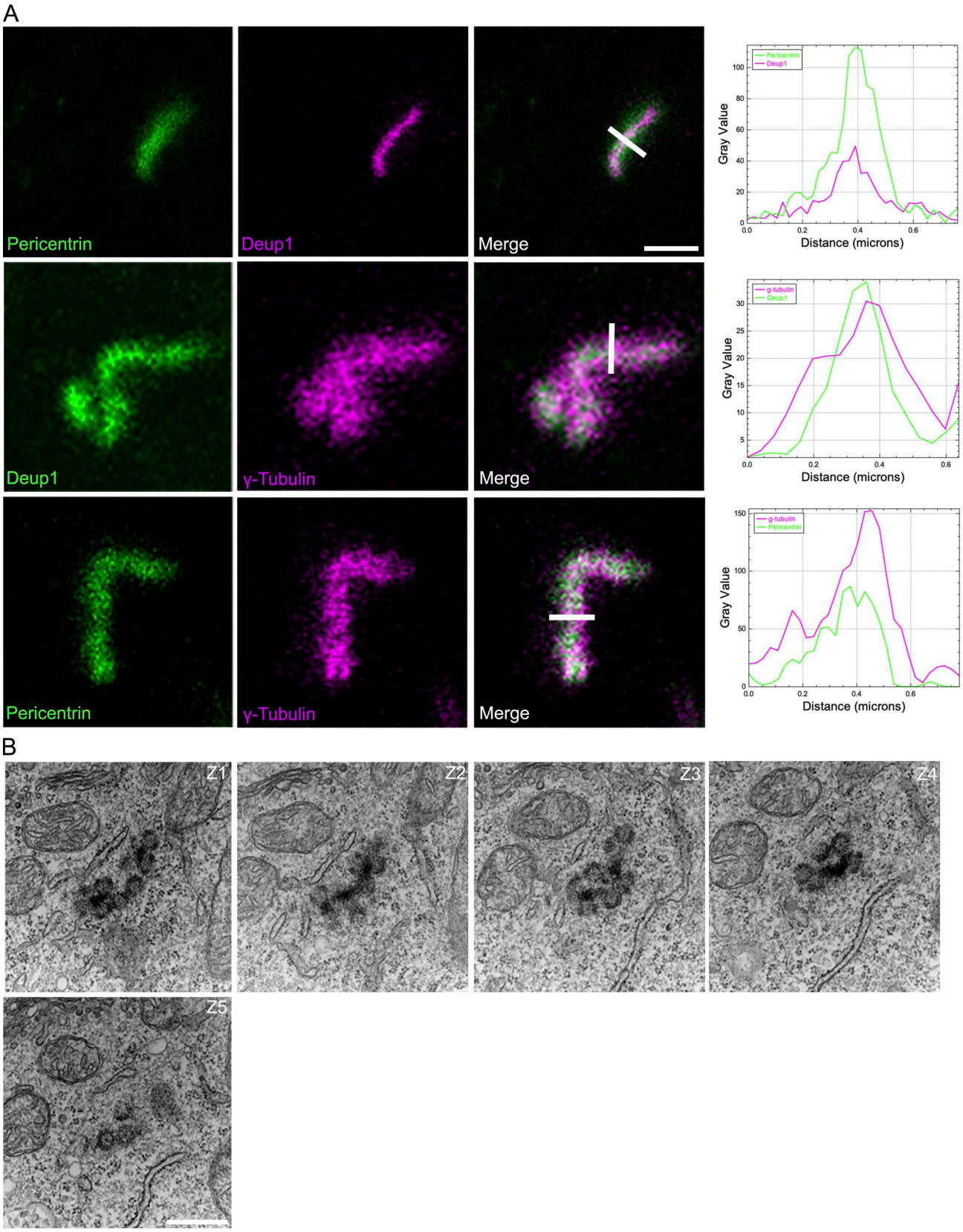

Figure S4. **STED and TEM analyzis of A6-MCI deuterosomes. (A)** STED super-resolution microscopy pictures of A6-MCI deuterosomes revealed by the indicated markers. The graphs plot mean intensity grey values for the indicated labelling, thus revealing the relative distribution of the corresponding proteins. **(B)** TEM pictures of consecutive 70 nm sections through deuterosomes of an A6-MCI cell. Z2 picture is duplicated in Fig. 4. Scale bar: 100 nm (A); 500 nm (B).

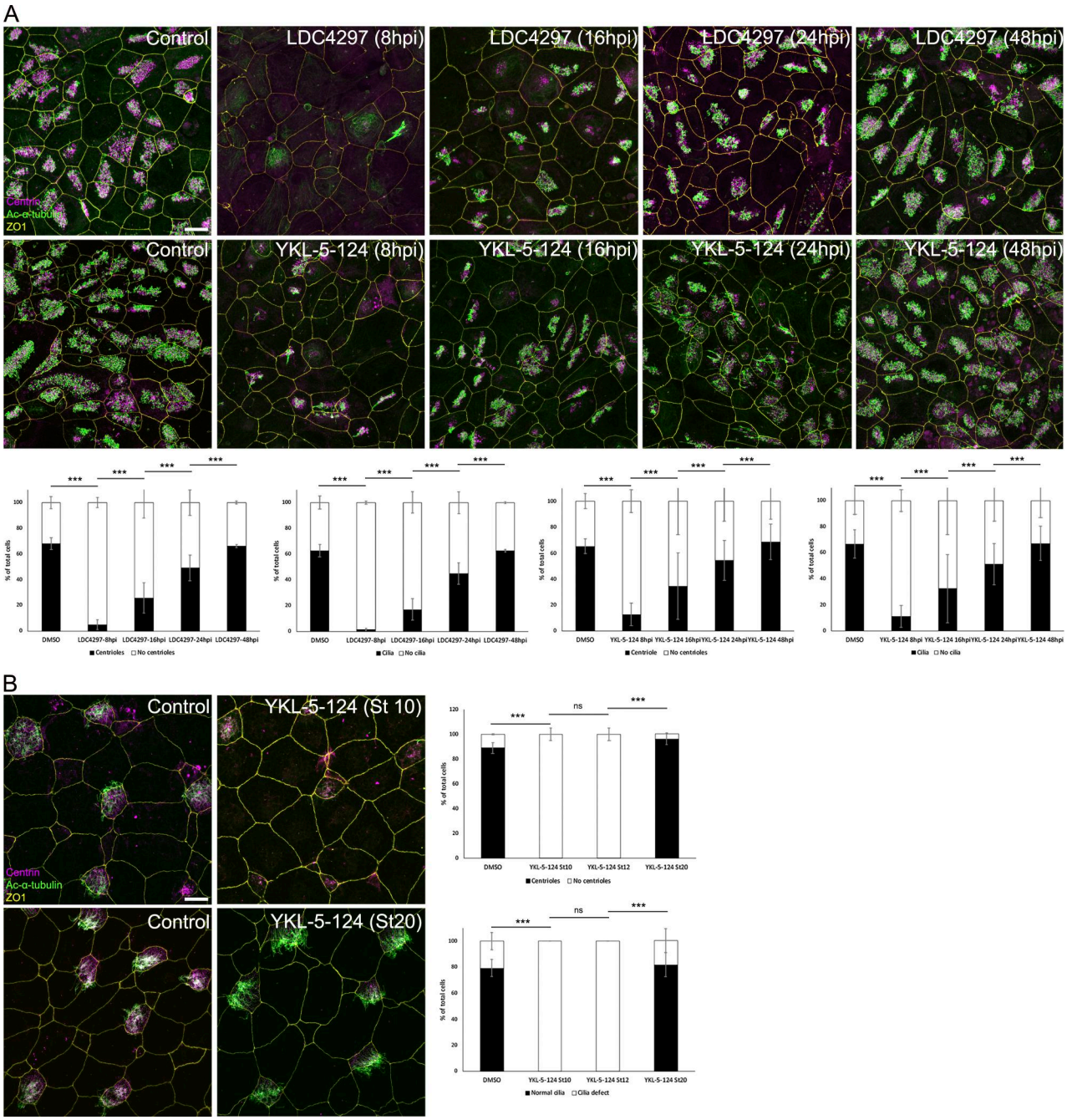

Figure S5. **Time-course analyzis of effet of CDK7 inhibition on A6-MCI cells and Xenopus embryos. (A)** Confocal pictures of A6-MCI cells treated with DMSO (control), LDC4297, or YKL-5-124 at the indicated hpi and immunostained for centrin (centrioles), Ac-α-Tub (cilia), and ZO1 (tight Junctions) at 72 hpi. Graphs show quantification of the phenotype. DMSO *n* = 508; LDC4297 *n* = 452 (8 hpi), 492 (16 hpi), 530 (24 hpi), and 502 (48 hpi); and YKL-5-124 *n* = 494 (8 hpi), 527 (16 hpi), 526 (24 hpi), and 622 (48 hpi) cells. SEM is shown. Data were collected from three independent experiments. Fisher's exact test: P < 2.2e−16 (***) for all comparisons. **(B)** Confocal pictures of *Xenopus* epidermis cells treated with DMSO (control) or YKL-5-124 at the indicated embryonic stages and immunostained for centrin, Ac-α-Tub, and ZO1 at stage 27. Graphs show quantification of the phenotype. DMSO *n* = 125 (DMSO) and YKL-5-124 *n* = 124 (St10), 141 (St12), and 160 (St20) cells. SEM is shown. Data were collected from three independent experiments. Fisher's exact test: P < 2.2e−16 (***) for DMSO vs YKl-5-124 (St10), YKl-5-124 (St12) vs YKl-5-124 (St20); P = 1 (ns) for YKl-5-124 (St10) vs YKl-5-124 (St12).

Video 1. **Time-lapse epifluorescence microscopy recording (20 fps) of fluorescent microbeads released at the surface of a control *Xenopus* embryo or A6-MCI cells at 72 h after induction.** On embryos, beads displayed continuous unidirectional movement. In contrast, at the surface of A6-MCI cultures, beads did not exhibit active movement but rather passive diffusion, suggesting that cilia were unable to beat.

Video 2. **Confocal live recording (1 picture/3 sec) of control (mRFP) or MCI-induced (mRFP + MCI) *Xenopus* epidermis.** In contrast to control cells, MCI-induced MCCs show little or no beating activity.

Video 3. **Tomogram acquisition and 3D tomogram reconstruction of a short deuterosome.** The deuterosome core is shown in green, and centrioles are in magenta.

Video 4. **Tomogram acquisition and 3D tomogram reconstruction of a long deuterosome chain.** The deuterosome core is shown in green, and centrioles are in magenta.

Video 5. **Tomogram acquisition and 3D tomogram reconstruction of a ramified deuterosome chain.** Deuterosome core is shown in green, and centrioles are in magenta.

Provided online is Table S1. Table S1 shows lists of proteins differentially expressed by A6-MCI cells between consecutive time points after induction.